energies

Review

CFD Modeling of Thermoacoustic Energy Conversion: A Review

Armando Di Meglio and Nicola Massarotti *

Department of Engineering, University of Naples "Parthenope" Centro Direzionale, Isola C4, 80133 Naples, Italy; armando.dimeglio001@studenti.uniparthenope.it
* Correspondence: nicola.massarotti@uniparthenope.it

Abstract: In this article, a comprehensive review of the computational fluid dynamics (CFD)-based modeling approach for thermoacoustic energy conversion devices is proposed. Although thermoacoustic phenomena were discovered two centuries ago, only in recent decades have such thermoacoustic devices been spreading for energy conversion. The limited understanding of thermoacoustic nonlinearities is one of the reasons limiting their diffusion. CFD is a powerful tool that allows taking into consideration all the nonlinear phenomena neglected by linear theory, on which standard designs are based, to develop energy devices that are increasingly efficient. Starting from a description of all possible numerical models to highlight the difference from a full CFD method, the nonlinearities (dynamic, fluid dynamic and acoustic) are discussed from a physical and modeling point of view. The articles found in the literature were analyzed according to their setup, with either a single thermoacoustic core (TAC) or a full device. With regard to the full devices, a further distinction was made between those models solved at the microscopic scale and those involving a macroscopic porous media approach to model the thermoacoustic core. This review shows that there is no nonlinear porous media model that can be applied to the stack, regenerator and heat exchangers of all thermoacoustic devices in oscillating flows for each frequency, and that the eventual choice of turbulence model requires further studies.

Keywords: thermoacoustic; computational fluid dynamics; porous media; renewable energy; oscillating flow

check for updates

Citation: Di Meglio, A.; Massarotti, N. CFD Modeling of Thermoacoustic Energy Conversion: A Review. *Energies* **2022**, *15*, 3806. https://doi.org/10.3390/en15103806

Academic Editor: Jose A. Almendros-Ibanez

Received: 10 April 2022
Accepted: 20 May 2022
Published: 22 May 2022

1. Introduction

Thermoacoustics is a multidisciplinary topic because it involves fluid dynamics, heat transfer, acoustics, solid mechanics and electrical engineering. The thermoacoustic effect was studied by Rayleigh for the first time in the XIX century by observing that pressure waves can be amplified if they interact in phase with an oscillating heat flux [1]. Thermoacoustic oscillations represent a critical issue for the aerospace industry because high-amplitude pressure oscillations produce significant mechanical stresses on engines and therefore must be prevented [2,3]. On the other hand, in recent decades, thermoacoustics has become increasingly attractive for the energy sector. In fact, the interaction between the fluid and solid matrix within a porous material, along which a certain temperature gradient is applied, can replicate the above oscillations to convert heat into electricity. At the same time, starting from the working fluid oscillations, a temperature gradient could be generated along the porous sample to obtain cooling power from electricity. Based on these principles, thermoacoustic devices can be used to obtain electricity or for cooling by exploiting waste thermal energy [4–6]. The use of a working fluid with a zero-greenhouse footprint, such as air, helium and argon, and the low capital and maintenance costs (due to the absence of moving parts) make this technology potentially very competitive with other technologies for energy conversion.

Thermoacoustic devices can be classified according to two different criteria: based on thermodynamics, they can be called thermoacoustic engines (TAEs) or thermoacoustic refrigerators (TARs), depending on acoustic principles. In this case, if the time phase shift between the acoustic pressure and velocity is approximately 90°, the working fluid experiences a thermodynamic cycle in the presence of a standing wave (SW). If the pressure and velocity are in phase, the working principle of the device is based on a traveling wave (TW).

The most recent physical prototypes of both TAEs and TARs have shown that electric and cooling power of about 5 kW can be reached [7]. Nevertheless, the dissemination of these devices is still limited to specific research applications, due to the very challenging design, and the complex interaction between the disciplines involved. For instance, with regard to thermoacoustic coupling, the classical linear thermoacoustic theory (based on which most devices are designed) is no longer valid when the acoustic pressure is roughly 10% of the operating static pressure, due to the occurrence of nonlinear effects. Not all causes of these phenomena are fully clear, despite the first experimental observations and consequent numerical models. However, it is known that these nonlinear effects impact negatively on the performances of thermoacoustic devices [8]. Computational fluid dynamics (CFD) models can be useful to describe thermoacoustic phenomena, by taking into consideration possible nonlinear effects, intrinsically not predictable by linear theory. A full CFD model of every component of a thermoacoustic device (stack or regenerator as a porous sample, heat exchangers, acoustic resonators, etc.) at the microscopic scale is still extremely computationally expensive, due to the presence of a large range of length scales: from the smallest, the viscous and thermal boundary layers, whose order of magnitude is 10^{-4} m, to the characteristic length of the whole device (1 m). Therefore, the use of macroscopic porous media models for parts of the thermoacoustic core (made up of heat exchangers and a stack/regenerator) can avoid the simulation of the smallest scales and reduce computational costs. However, the increase in computational power could make this approach more competitive in the near future, both in the design/analysis phase and for the understanding of all physical phenomena that occur outside the linear theory description [8].

In recent decades, several review articles have been published in the field of thermoacoustics. Mainly, these reviews concern general thermoacoustic principles and applications [9,10], the coupling between acoustics, heat transfer and solid mechanics [11], or specific types of thermoacoustic devices such as traveling waves [5,12] or standing waves [13]. In terms of numerical modeling, the book of Swift [8] and the guide of the open-source software DeltaEC [14] are available on linear theory. Despite the number of scientific articles that have adopted CFD tools to model thermoacoustic devices, a comprehensive review of this approach is not still available, according to the authors' knowledge.

The present work aimed at analyzing how CFD-based models have been applied in the thermoacoustic field. Such work is necessary due to the broad range of setups, boundary conditions and sub-models currently employed in the available literature.

The outline of this paper is organized as follows. In the next section, an overview of the modeling approach used in thermoacoustics is presented, from lumped models to the CFD approach, by analyzing typical simulations and the advantages/disadvantages of each method. The third section describes the physical phenomena that can only be modeled with a CFD approach. In the fourth section, all CFD-based models investigated in the literature are analyzed in terms of computational domains (a single thermoacoustic core or a full thermoacoustic device), different boundary conditions, turbulence models and other modeling approaches adopted. The last section of the paper presents some conclusions and a future outlook.

2. Thermoacoustic (TA) Modeling Approaches

The domain in which they are developed, i.e., the time or frequency domain, is the main parameter to classify models in thermoacoustics. Acoustics, dealing with oscillating flows, is mostly described in the frequency domain. Generally, these models are based on the linearity hypothesis, because they assume that each quantity oscillates with a sinusoidal trend during a period. Consequently, transient phenomena leading to the periodic steady state cannot be captured. On the other hand, a time-domain approach allows simulating these effects, but it is clearly more expensive in terms of computational costs. An overview of the TA modeling approaches is presented in Figure 1.

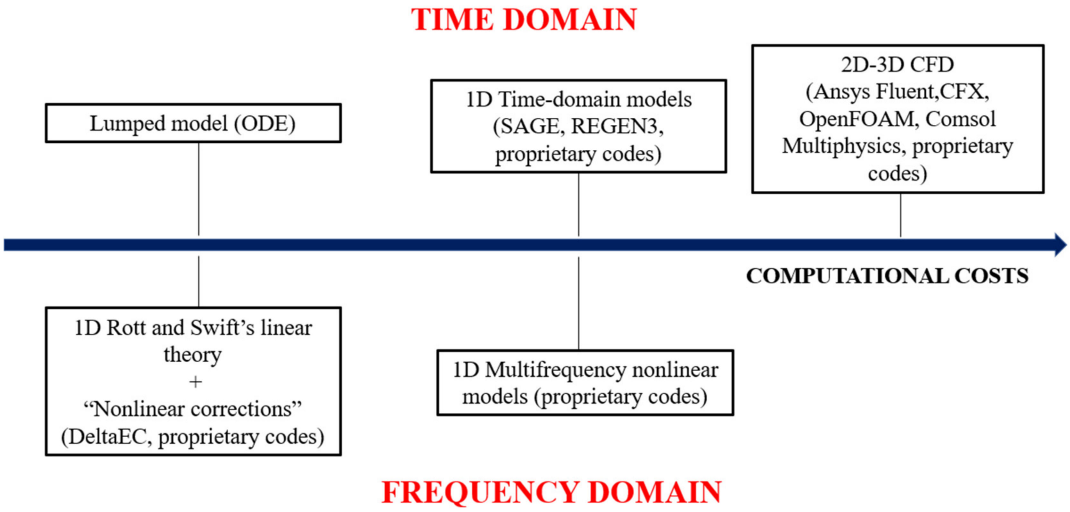

Figure 1. Overview of modeling approaches in thermoacoustics.

2.1. Linear Thermoacoustic Theory (LTT)

The most widespread modeling approach is linear thermoacoustic theory (LTT), a 1D model initially developed by Rott [15] and integrated by Swift [16], used as a design and analysis tool for full thermoacoustic devices, implemented in the open-source software DeltaEC [14]. The mathematical model is based on three equations: continuity, momentum for the pressure p_1 and volumetric flow rate U_1 (as complex variables) and a total energy equation for the mean temperature distribution T_m. These can be derived under the assumption of "Rott's acoustic approximation", expressing each variable as a steady-state component and a time-dependent fluctuation, introducing them in the Navier–Stokes equations (NSE) and canceling higher-order terms. The first-order continuity and momentum equations in the frequency domain are reported below with an interesting electroacoustic analogy, where each component of a thermoacoustic device can be fully characterized by a viscous resistance r_v, inertance l, thermal relaxation $1/r_k$, a compliance c and a controlled source term g depending on the mean temperature gradient, as presented in Figure 2. This electrical analogy can be naturally extended to also take into account, with an equivalent impedance, the electromechanical coupling due to the presence of a speaker or a piezoelectric device to provide or absorb acoustic power [17,18].

$$\begin{aligned} \frac{dU_1}{dx} &= -\left(1+\frac{\gamma-1}{1+\epsilon_s}f_k\right)\frac{i\omega A}{\gamma p_m}p_1 + \frac{f_k-f_v}{(1-\sigma)(1+\epsilon_s)(1-f_v)}\frac{1}{T_m}\frac{dT_m}{dx} \\ &= -\left(i\omega c+\frac{1}{r_k}\right)p_1 + gU_1 \\ \frac{dp_1}{dx} &= \frac{i\omega\rho_m}{(1-f_v)A}U_1 = -(i\omega l + r_v)\,U_1 \end{aligned} \tag{1}$$

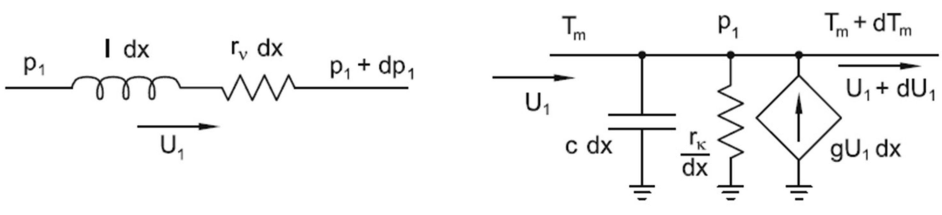

Figure 2. Electroacoustic analogy for linear continuity and momentum equations [8].

The thermo-viscous functions (f_k, f_v), depending on the ratio between the hydraulic diameter and thermal-viscous penetration depths, macroscopically describe the thermal and viscous losses for a porous sample, or simply the boundary layer effects in an acoustic resonator. The ϵ_s parameter takes a finite solid thermal capacity into consideration [19], σ is the Prandtl number and γ is the ratio of specific heats of the fluid.

The main advantage of LTT is the small computational costs, meaning that the software can be run to quickly perform large parametric analyses and optimizations. LTT numerical results are in good agreement with experimental data until the pressure amplitude is roughly lower than a tenth of the static operating pressure [20]. Moreover, based on the same theoretical model, it is possible to study linear thermoacoustic stability, the relation between the onset temperature of the acoustic oscillations and their frequency and the initial growth ratio, with satisfying accuracy [21]. The acoustic growth ratio is a fundamental parameter to be taken into account in the design phase for the startup of the engine. It is analytically related to the imaginary part of the complex frequency and the ratio of two consecutive peaks of the pressure (or velocity) time history. When it is negative, an external acoustic perturbation can exponentially increase in amplitude; otherwise, it decreases until the quiescent state [22]. The main drawback is the inability to consider all nonlinear phenomena that will be described in the next section.

2.2. Two-Dimensional Model in Frequency Domain

A similar linear thermoacoustic stability was also presented by De Jong et al. with a 2D model, based on the finite element method, representing a standing-wave engine [23]. For different temperatures prescribed at the hot heat exchanger, the complex frequency was calculated, as well as the minimum temperature needed to start up the engine. Compared to a 1D model in the frequency domain, such an approach allows predicting the acoustic velocity and pressure distribution potentially better at the interface of two different components. Furthermore, a 2D temperature field can predict the heat exchanged in the transversal direction, while for a 1D model, time-averaged thermal power is present only in the heat exchangers by directly prescribing it or using a third type of boundary condition. However, to the authors' knowledge, an evaluation of the balance between the advantages coming from a 2D field of the variables and the consequent higher computational costs of a 2D approach has never been realized.

2.3. Multi-Frequency Domain Approach

In addition to the previous linear method, other models were built to work not only at the fundamental frequency but also with its harmonics. Muralidhar and Suzuki [24] proposed a frequency-domain approach using fourth-order harmonics, thermal non-equilibrium and the Darcy–Forchheimer model recovered by porous media theory for stationary flows [25]. The results in terms of the equivalent friction factor and dimensionless complex pressure drop were shown. In this model, the harmonics did not interact with each other. Conversely, in [26], a second-order approximation technique was used by taking into account the first-order unsteady term, the second-order steady term and the second-order unsteady term. A thermal non-equilibrium model using Nusselt number correlations was employed, as well as the permeability and Forchheimer coefficient for the regenerator, even if the numerical correlations for modeling the viscous and inertial losses were not presented. The results expressed in terms of the numerical friction factor were compared with the experimental data of Tanaka [27]. Regardless of the specific coefficients adopted for modeling the porous core and the calculation of the numerical friction factors, such a model contains the approximation of the nonlinear convective term in the momentum equation.

Moreover, De Jong et al. [28] proposed another nonlinear model in the frequency domain, based on the quasi-1D time-domain-based model of Prosperetti et al. [29], considering six harmonics. The heat transfer and momentum terms were modeled with the linear exact solution, while the temperature wall distribution was prescribed (and constant over time). This model converged only above the onset temperature, so the frequency was calculated as that corresponding to the minimum temperature difference along the wall stack for which the simulations converged.

2.4. Lumped and 1D Time-Domain Models

Prosperetti built a 1D unsteady model aimed at predicting the thermoacoustic instability phenomena from the startup to the limit cycle in a standing-wave thermoacoustic engine [29–32]. This model, derived from the integration on the coordinate orthogonal to the wave propagation, macroscopically takes into account the momentum and heat transfer terms in the stack, well described by the thermo-viscous functions f_v, f_k in the linear regime. At startup, in the linear regime, the model perfectly matches the results of Rott and Swift's model [16]. For a larger amplitude, when the nonlinear saturation takes place, analytical solutions do not exist, and an approximation is proposed for the drag and heat transfer terms by adding convective-like terms in the momentum and energy equations. The main issue is the instability of the model because it numerically amplifies acoustic modes that are damped. This is related to the fact that, in a time-domain formulation, the frequency used to calculate thermo-viscous functions is chosen a priori. The authors proposed a heuristic but effective method, by using a value very close to the analytical solution of the angular frequency combined with artificial damping in the energy equation. The wall temperature in the first two papers by Prosperetti is considered constant with time, implicitly assuming that the solid medium has a much higher thermal capacity compared to the fluid one. In a later work, Prosperetti et al. [31] generalized the source terms in the transport equations considering closure parameters variable with the velocity, by solving additional ordinary differential equations (ODEs) for these parameters. The method, even if it does not have a physical derivation, is more robust than the previous one because it does not need artificial damping. Another approach adopted by Karpov and Prosperetti [33] to study the nonlinear saturation instability consists in the perturbation expansion of the variable to the fourth order (energy related to the first-order variable is a second-order quantity, while to take into account energy dissipated by the second-order variable, an approximation up to fourth order is needed), showing as results the trends in the dynamics of the pressure amplitude from startup to saturation. This approach is based on the evidence that the time scale of the resonance standing wave differs from the time scale of the startup and nonlinear saturation.

On the other hand, Wang et al. [34] focused on the onset characteristics of a traveling-wave device. The thermo-viscous functions were used to model viscous and thermal relaxation effects in the resonator and the heat exchangers (HXs), while for the screen-type regenerator, the viscous losses were taken into account with the friction factor correlation, defined by Swift in [35], depending only on the porosity of the medium. Such a model is not effective to predict the amplitude of the limit cycle because it underestimates all nonlinear losses, net streaming, minor losses, etc. In fact, the amplitude reached with such a model is too high compared with experimental data because such losses are neglected [34]. The paper shows the importance of the thermal relaxation effects to correctly evaluate the amplitude of the limit cycle. If they are neglected, the amplitude of the limit cycle is even greater than when they are taken into account. Note that, as before, a time-domain model which uses frequency-dependent parameters, such as the thermo-viscous functions, requires specifying, firstly, the frequency, calculating the results and eventually updating the parameters and re-calculating with the numerical frequency found, until the convergence loop is reached.

The nonlinear effects caused by Rayleigh streaming are among the reasons for overestimating the amplitude. These effects were taken into account by Penelet et al. [36] in order to simulate a realistic limit cycle. They implemented a simplified lumped model, made of a system of ODEs, for describing the heat transfer process and pressure amplification. Similarly, Zare and Tavakolpour-Saleh [37] proposed another simplified lumped model, composed of only two single ODEs/degrees of freedom for a single-stage thermoacoustic Stirling engine equipped with two mechanical membranes. The nonlinear dynamics of the phenomena were included in the cubic correlation for the spring stiffness of the diaphragms. These correlations, as well as the damping coefficients and the flow resistance, were obtained experimentally thanks to pressure and displacement measurements.

Matveev [38], instead, developed a lumped thermal capacity model, mathematically described by an ODE system of energy balances for the stack and heat exchangers. Such a model considers a nonlinear damping coefficient related to all losses as an input to obtain a realistic limit cycle amplitude.

Penelet et al. [39] built a 1D model based on three partial differential equations (fluid, solid, resonator temperature) and three ordinary differential equations (streaming velocity and first/second-order acoustic pressure) to describe the engine operation from the startup to the limit cycle, passing through nonlinear saturation. Numerical results, taking the acoustic streaming, higher harmonics generation and minor losses into consideration, agree with experimental data.

Guedra et al. [40] constructed a hybrid model between the time domain and frequency domain to calculate the pressure dynamic evolution. They calculated the pressure, its amplification factor and temperature distribution along the stack from a first-order ODE, an eigenvalue problem in the frequency domain and a 1D unsteady energy equation, respectively.

Boroujerdi and Ziabasharhagh [41] simulated a pulse tube refrigerator (equipped with a wire screen regenerator) driven by a standing-wave engine equipped with a parallel plate stack using 1D unsteady NSEs. Macroscopic thermal and fluid flow characteristics were described by the friction factor and Nusselt number, respectively.

Sun et al. [42] developed a nonlinear mathematical model of NSEs solved with the finite difference method for a three-stage traveling-wave engine. Different steady-state correlations of the friction factor and Nusselt number were used for the pipe (fully turbulent), regenerator (from the classical Stirling engine literature) and heat exchangers (rectangular channel). The results, compared against experimental data, showed a gap in the fundamental harmonic pressure. The authors attributed it to the underestimation of streaming phenomena (see Section 3.3.2). However, the Gedeon streaming, being caused by a second-order static pressure gradient, could be predicted by such a 1D time-domain nonlinear model.

Developing novel numerical models is not the only possibility to simulate thermoacoustic devices with 1D models in the time domain. In fact, Luo et al. [43] performed a numerical simulation of a heat-driven free-piston thermoacoustic-Stirling refrigeration system with "SAGE" software [44]. Such software works with an unsteady nonlinear model setup using four equations: continuity, momentum and energy for the 1D fluid flow, and Newton's law for the displacer, treated as a mass-spring-damper system forced by the pressure difference between the compression and expansion chambers. Both heat exchangers and mesh screen regenerators were modeled with the friction factor and Nusselt number correlations in laminar and turbulent regimes. Similarly, Li et al. validated and numerically optimized a coupled engine-refrigerator system using SAGE [45]. Another software working similar to SAGE is the 1D software REGEN3 [46], which was used to carry out a parametric analysis of a thermoacoustically driven refrigerator in [47].

2.5. CFD-Based Approach

Acoustic, thermoacoustic and, more generally, aeroacoustic phenomena can be described by the Navier–Stokes equations. Aeroacoustics represents a numerical challenge because pressure and velocity acoustic oscillations are very difficult to capture in the presence of complex flows. For example, in the aerospace sector, the obvious presence of a mean time flow makes the impact of the acoustic oscillations on the fluid flow irrelevant, even if such oscillations cause aerodynamic noise. On the other hand, in the field of thermoacoustic energy conversion, the mean flow is an unwished consequence of nonlinear losses. In this framework, the oscillating component of the velocity is ideally much higher than the steady-state component. At most, the latter, in the presence of a net mass flow rate, can have the same order of magnitude as the fluctuation component. Therefore, traditional methods based on CFD can be applied to thermoacoustics without invoking the above numerical difficulties of aeroacoustics. A CFD-based approach is undoubtedly the most expensive, but it allows capturing most of the phenomena that strongly affect the performance of a thermoacoustic device, not predictable by the previously described approaches. These phenomena, for simplicity and a better understanding, can be classified into three categories: acoustic (harmonics and shock waves), dynamic and hydrodynamic nonlinear losses [11].

3. Nonlinear Phenomena in Thermoacoustics

3.1. Acoustic

3.1.1. Harmonics

Wave distortions from a purely sinusoidal pattern can be attributed to the presence of other frequencies in addition to the fundamental one, as shown in an example in terms of the time pressure history and its frequency spectrum (Figure 3a,b). Acoustic pressure harmonics, as a result of nonlinear wave propagation or excitation of harmonic modes, can significantly arise when the ratio between the amplitude at the fundamental frequency and the operating frequency (drive ratio, Dr) is higher than 10% [20]. In addition, thermal wave distortions were also observed for lower values of Dr [48], but the energy dissipation they carry can be neglected because it contributes as a fourth-order term, significant in the energy balance only at a high Dr [8].

3.1.2. Shock Waves

If the above pressure harmonics are not suppressed using anharmonic tubes as suggested in [49], in the presence of a very steep temperature gradient along the stack/regenerator, the same harmonic can degenerate into periodic shock waves (Figure 3c). These were first observed experimentally and then replicated numerically [50–52]. Both approaches confirmed that such phenomena are rarely found in real thermoacoustic devices, as confirmed by the efforts they made to reproduce them experimentally [49].

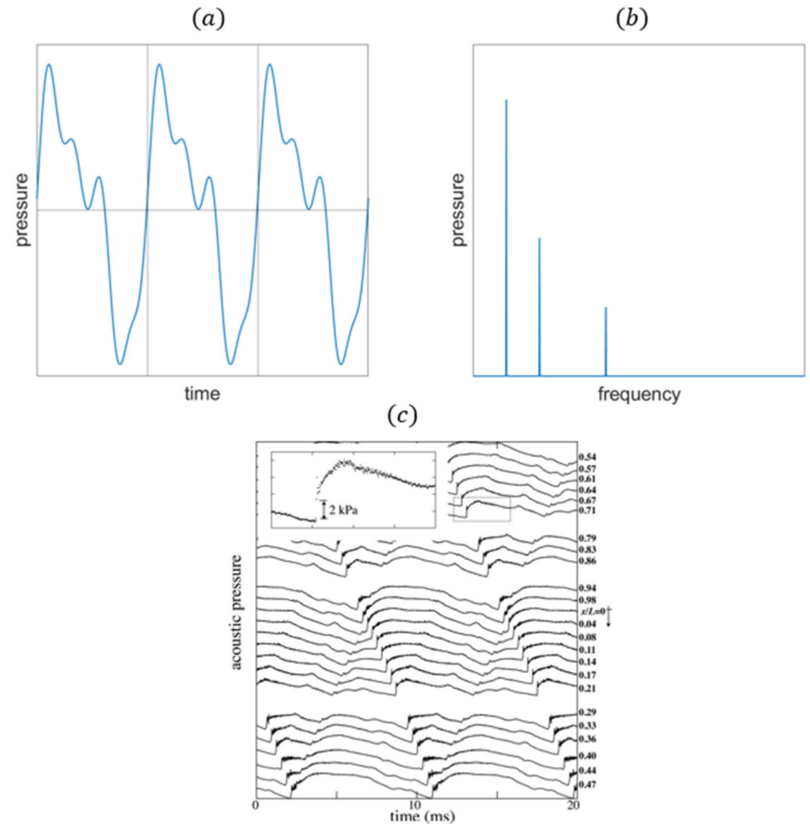

Figure 3. Harmonics in the time domain (**a**) and frequency domain (**b**), and shock waves (**c**) [53].

3.2. Dynamic

According to dynamic system theory, a thermoacoustic engine is a system that is in the presence of external perturbation responses at the natural frequencies. If the temperature prescribed at one end of the stack (or the high-temperature heat exchanger) overcomes a threshold value called T_{onset}, pressure oscillations arise. These increase exponentially to a saturation phase, where nonlinear losses begin to limit the exponential growth, and a dynamic balance between generation acoustic power produced and viscous dissipation is reached [54], as shown in Figure 4. Generally, three natural frequencies at most are involved in this dynamic process. Obviously, only the unstable modes exponentially increase in amplitude, while the stable ones decay. While the initial growth (decay) is well described by LTT, only a nonlinear approach can describe the saturation process where the excited frequencies interact with each other. The limit cycle could be characterized by a single frequency oscillation or by a more complex dynamic response such as beating (Figure 5a), quasi-periodic oscillations (Figure 5b) or even chaotic oscillations (Figure 5c) when more than one frequency is involved [55,56]. For a steeper temperature gradient, the second harmonic can completely dominate the fundamental one (mode transition phenomenon) [57]. Additional nonlinear patterns not reported here are the overshoot (local maximum of the pressure amplitude and, following that, a slight increase towards the limit cycle) and the double-threshold effect (the first saturation does not lead to a limit cycle but to another exponential growth). Such a nonlinear dynamic system can depend on the initial conditions. More specifically, between the onset temperature and the so-called "damping temperature", the system can reach both a limit cycle and a quiescent state, depending on the initial conditions [58]. Furthermore, additional nonlinear characteristics have been discovered between the damping and onset temperatures from an experimental perspective: on–off (surging–quenching) oscillations and Fishbone-like instability. The surging–quenching phenomenon occurs when a threshold operating pressure is overcome [59], while the Fishbone-like nonlinearities are qualitatively described and attributed to the complex interaction between the acoustics and temperature field [60].

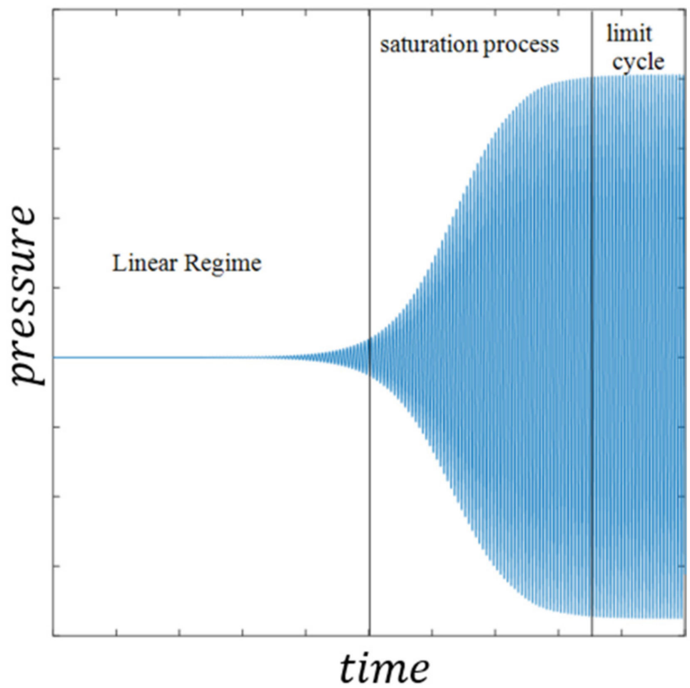

Figure 4. Typical dynamics of pressure oscillations for a thermoacoustic linear regime (exponential rise), saturation process and limit cycle.

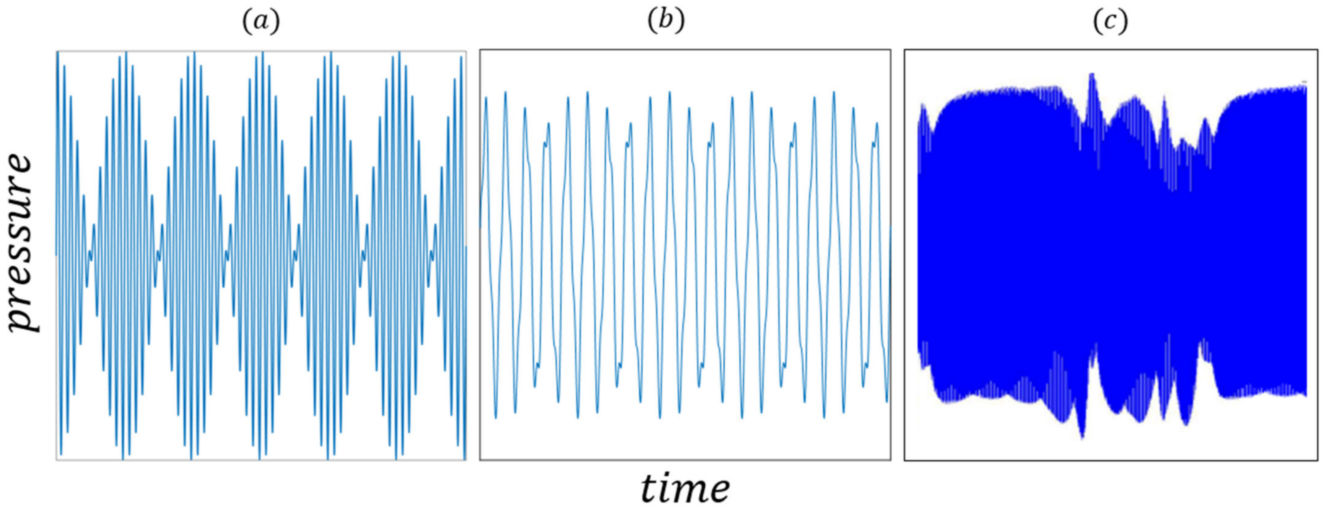

Figure 5. Beating (**a**), quasi-periodic oscillations (**b**) and chaotic oscillations (**c**).

3.3. Hydrodynamic

3.3.1. Turbulence

In a turbulent and steady pipe flow, it is well known that the friction factor depends on the Reynolds number and roughness of the pipe. In oscillating flows, another dimensionless parameter, related to the frequency, must be introduced. Possible choices to account for the oscillating inertial force compared to the viscous one are the ratio between the hydraulic diameter and viscous penetration depth or the Reynolds number with the viscous penetration depth as the length scale, or the Valensi (Va) or Womersley numbers (Wo) [61]. While, in a steady-state flow, the laminar transition and fully turbulent regions are well studied and clearly defined, in oscillating flows, there is only a qualitative description of the thresholds between laminar and "weakly turbulent", and "conditionally turbulent" and "fully turbulent" regimes [8]. The laminar regime is well described by linear theory, which can also apply to the weakly turbulent flow regime because turbulence does not perturb the boundary layer in this case. In conditional turbulent flow, high-frequency fluctuations occur during the deceleration phase and then the flow tends to be more laminar, becoming weakly turbulent. At higher Reynolds numbers, the flow becomes fully turbulent because the boundary layer is also disturbed by turbulence bursts for the whole acoustic period. Swift summarized the findings of all regimes in oscillating flows based on the experimental results of Hino et al. [62]. The qualitative chart in Figure 6, with the Reynolds number as the horizontal axis, calculated as $\rho D_h u/\mu$, and the ratio between the hydraulic diameter D_h and the viscous penetration depth δ_v as the vertical axis, illustrates the above-mentioned turbulent regimes in oscillating flows, with examples of the velocity wave detected experimentally by Hino et al. [62] with an anemometer for each region.

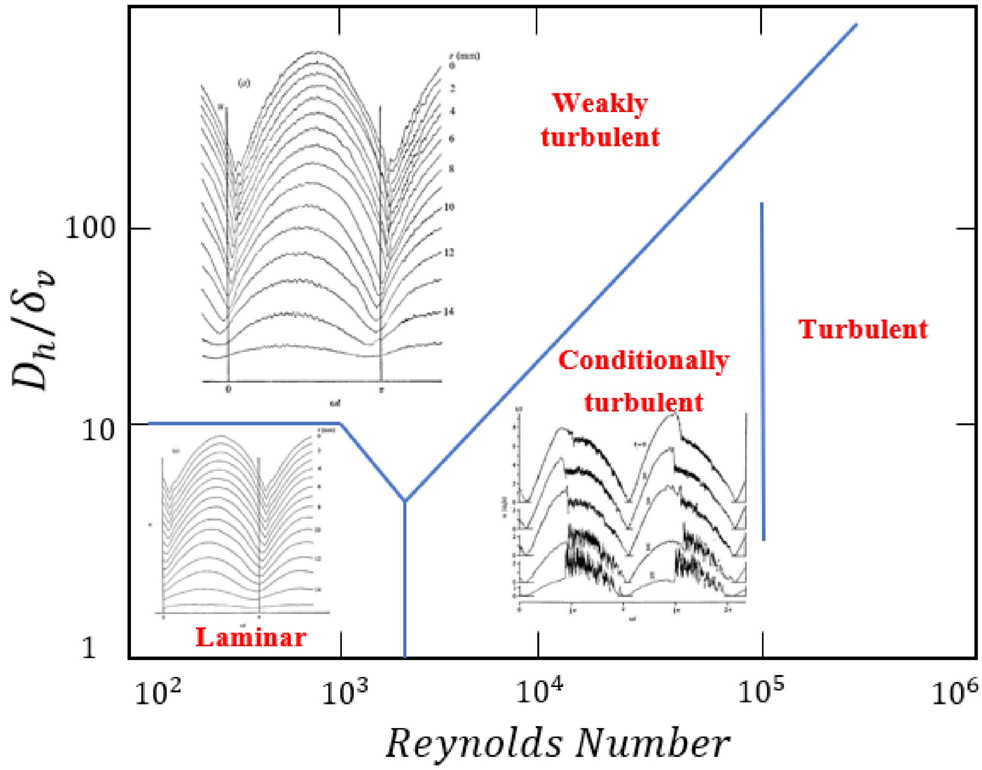

Figure 6. Qualitative boundaries of turbulent regimes in oscillating flows based on the results of Hino et al. [62] and Swift's reproduction [8]; velocity waves are always positive because an anemometer cannot detect the oscillating flow direction.

In general, most experimental investigations were conducted in the 1990s [63,64], while numerical analyses instead were provided by Feldmann and Wagner's direct numerical simulation results more recently [61]. However, both experimental and numerical results represent only a few operating conditions and do not allow confirming and gaining deeper insights regarding the content in Figure 6.

In a DeltaEC-based linear model, the effects of turbulence are taken into account in empty pipes (ducts and cones) by invoking "Iguchi's hypothesis", according to which the flow has no memory of its recent history. With this assumption, oscillating flows can be considered in each instant of time as stationary ones. It is a quite valid assumption, such as for the application of steady-state correlations for regenerators, in the low-frequency limit ($r_h < \delta_v$). In practice, in the framework of the five-parameter model presented in Figure 1, the viscous resistance r_v is enhanced (taking into consideration the turbulence effects through a coefficient m_v related to the steady-state Moody friction factor). Likewise, for heat exchangers, a coefficient m_k has been introduced to consider the effects of turbulence on heat transfer. For $r_h/\delta_v < 2$ (low-frequency limit), the coefficients (m_v, m_k) are assumed to be 1 up to $Re \approx 2000$, as in steady-state pipe flow. On the other hand, for $r_h/\delta_v < 2$, the transition Reynolds number depends on the frequency. The higher the frequency, the larger the critical Reynolds number will be, $Re \approx 2000\ r_h/\delta_v \propto \sqrt{Va}$. In terms of the Reynolds number based on the viscous penetration, the threshold value to consider the transition from laminar to turbulence ranges from 400 to 500. Similar considerations to consider the effect of turbulence in oscillating flows have been taken into account in the 1D time-domain software SAGE [44]. Saat and Jaworski performed CFD numerical prediction of early-stage turbulence in oscillatory flow across a parallel-plate HX [65]. Three different turbulence models (SST $k-\omega$, SST transition $k-\varepsilon$) were investigated. The SST $k-\omega$ model provides the best fit to experiments in terms of velocity data. A remarkable finding is the much lower critical Reynolds number found (between 70 and 100 and based on the viscous penetration depth) compared to the above higher values commonly accepted. However, this departure can be attributed to the end effects and vortex shedding phenomena characterizing a parallel-plate stack, while the above references are related to studies in empty oscillating pipe flow. Similar findings were also reached later by Huang and Jaworski [66]. Ramadan et al. [67] numerically confirmed the same value of the critical Re in oscillating pipe flow (500) as that of Merkly and Thomann's experimental [68].

Overall, two possible approaches can be found in the literature to consider the effects of turbulence: directly solving the Navier–Stokes equations or introducing a turbulence model. According to the first one, the use of homemade high-fidelity numerical schemes (especially if 3D) allows one to reproduce the transitional effects of the turbulence [69,70], without any additional model. Similarly, using a laminar model in commercial codes with fine meshes and time steps is also another strategy that has been used in works available in the literature. Such models behave like a LES because they at least attempt to solve the macroscale. By contrast, they do not use any sub-grid model, allowing the dissipation of the smallest turbulent vortices thanks to the numerical diffusion. They are also known as ILES (implicit large eddy simulation) in the literature [71,72]. On the other hand, the $k - \varepsilon$ turbulence models are by far the most widespread ones, probably for their applicability to a wide range of flows. In [73], for oscillating pipe flow, the authors found the use of the standard $k - \varepsilon$ acceptable, but only when the flow was fully turbulent. However, in the literature, there is no robust experimental evidence which indicates the best turbulence model to be adopted in thermoacoustics. Among the RANS models, the $k - \omega\ SST$ turbulence model seems to best fit the experimental data. Further studies and experimental campaigns should be aimed at assessing when the laminar–turbulent transition occurs and evaluate the optimum turbulence model in a real thermoacoustic device. This is not a trivial issue or a merely theoretical question to solve, as Chen et al. [58] have shown that the pressure amplitude of the limit cycle of a standing-wave thermoacoustic engine can change dramatically (even by about a factor of 2) among the six turbulence models tested (laminar, $k - \varepsilon$ standard, $k - \varepsilon$ realizable, $k - \omega$ standard, $k - \omega$ SST). The use of LES, instead, is less common for its higher computational costs. Chen et al. [74] adopted it for a deeper understanding of minor losses, whereas Jaworski et al. studied entrance effects in oscillating flows [75]. Guo et al., in reproducing the same model studied by Chen et al. [74], found that, in terms of the pressure amplitude at the wall, the percentage difference between the LES result and $k - \varepsilon$ is approximately 10% [76]. A compromise between LES and RANS models is DES (detached eddy simulation), a hybrid method that solves the macrostructures of the turbulence if the mesh size is fine enough; vice versa, it behaves as a RANS model in the other cases [77]. However, in thermoacoustics, there are no examples of application of this turbulence model, considering the difficulties in generating an accurate grid due to such a shift between RANS and LES.

3.3.2. Mass Streaming

A nonzero time-averaged flow rate in a certain section of the domain, which superimposes to the oscillating first-order mass flow rate and is driven by the same first-order variables, is known as streaming in acoustics and thermoacoustics. In [78], a comprehensive review of streaming is presented. According to Swift's classification, four types of streaming can be identified, as pictured in Figure 7.

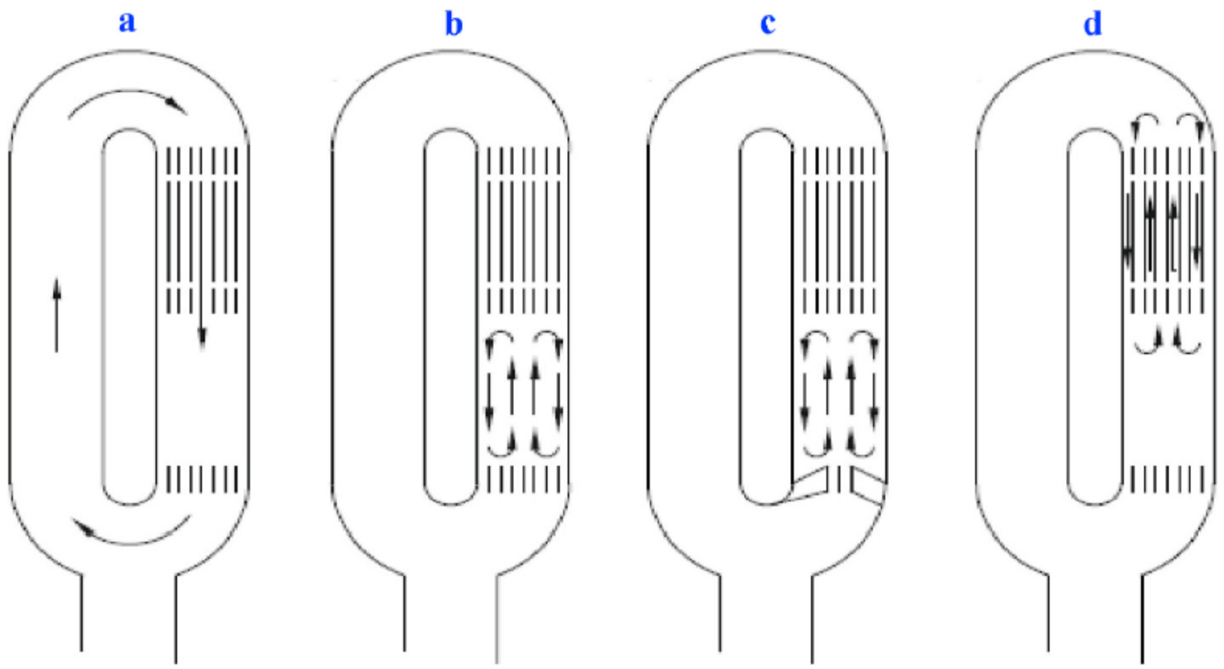

Figure 7. (**a**) Gedeon streaming, (**b**) Rayleigh streaming, (**c**) jet-driven streaming and (**d**) streaming with a regenerator or stack [8].

- Gedeon streaming

Gedeon streaming is promoted by a torus-shaped or looped geometry, and it causes a large averaged convective heat flux from the hot to the cold side of the regenerator (Figure 6a). On the other hand, for standing-wave devices, it is absent. It can be suppressed by introducing a deliberate minor loss to compensate for the mean time pressure drop driving such flow, as will be explained in the "Minor Losses" section below.

- Rayleigh streaming

Rayleigh streaming is a local nonzero mass flow rate driven by viscous/thermal boundary layer phenomena and the presence of a temperature gradient (Figure 6b). It can be suppressed by using a tapered tube. This phenomenon has been studied numerically by Oosterhuis et al. by including a no-slip wall, including specific oscillating source terms in the momentum equation to simulate a vibrating resonator [79].

- Jet-driven convection

The tube entrance as sudden expansion/contraction may bring about a steady jet. Generally, flow straighteners are used to cancel such jets. However, with a net mass flow rate, such as this one, streaming can sometimes be deliberate and exploited for heat transfer enhancement purposes. In fact, Chen et al. studied a deliberate jet formation driven by a thermoacoustic standing-wave device introducing a sudden contraction at the end of the resonator, with CFD simulations [80].

- Streaming with a regenerator or stack

There is little knowledge about the origin of this streaming type, but it is generally detrimental like the other types of streaming.

3.3.3. Minor Losses

In the case of the macroscopic model of the thermoacoustic core, the issue of the "minor losses" at the ends of this component should be carefully dealt with. It has already been mentioned that neglecting it leads to an overestimation of the acoustic pressure amplitude at the limit cycle [34]. The name "minor losses" in fact can be misleading because it relates to the acoustic approximation at a low amplitude, where they are negligible as they scale with the squared bulk velocity. The pictures in Figure 8 report the vorticity field near the right end of a parallel-plate stack taken from the article of Shi et al. [81], clearly showing the vortex shedding phenomena at one end of the parallel-plate stack for six different time frames (Figure 8a–f).

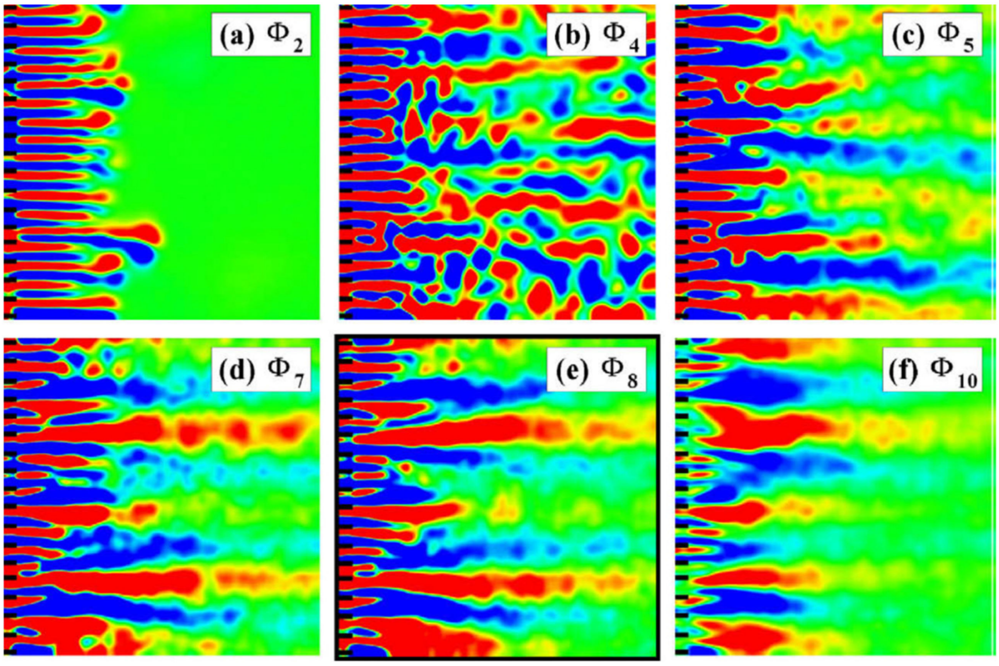

Figure 8. Typical minor loss at the ends of a parallel-plate stack [81] for six different time frames within an acoustic period (**a**–**f**).

In steady-state flow, they are generally known in the literature as "concentrated pressure drops". The coefficient K expresses the relation between the pressure drop and velocity and is known for sudden contraction, expansion, bends, etc.

$$\Delta p = \frac{1}{2A^2} K \rho U^2 \tag{2}$$

As for turbulence and macroscopic modeling of a regenerator, the previous equation can also apply to oscillating flows when the displacement amplitude is far larger than all the characteristic lengths, and the quasi-steady hypothesis is therefore invokable. Most of them are experimental [82], but there is no parametrization of the pressure drop in oscillating flow when $|\xi_1| \leq r_h$, making Equation (2) inadequate for oscillating flows.

For the first time, Swift adapted Equation (2) to be suitable for DeltaEC, by assuming a sinusoidal volumetric flow rate U and gaining the pressure drop Δp_{ml} as the first order of the Fourier transform:

$$\Delta p_{ml} = \frac{4}{3} \pi \frac{K \rho}{A^2} |U_1| U_1 \tag{3}$$

Equation (3) was also used by Lin et al. [70] to parametrize the minor loss in a 1D linear model to conduct an effective comparison with their CFD-based model of a standing wave with a parallel-plate stack. The loss coefficient was assumed to be equal to the sum of both steady-state expansion and contraction coefficients (K_{exp} and K_{cont}). Yiyi et al. [83] tried to characterize the loss coefficient K with a CFD-based approach, for the same stack–resonator discontinuity, revealing that K in turn depends on the flow field, as the authors' correlations showed. To the authors' knowledge, any correction similar to Equation (2) has not been applied to a regenerator in a CFD model yet.

A minor loss, instead, is deliberately designed in closed-loop thermoacoustic devices to suppress the so-called Gedeon streaming which strongly affects the performance of a thermoacoustic engine. There are many ways to induce this pressure drop, including the use of an elastic membrane, an orifice and a short tube. These must be sized to determine a steady pressure drop equal to that produced by the regenerator, with a clear opposite sign to block the streaming, trying to minimize the acoustic energy dissipation related to this pressure drop.

Lyklama a Nijeholt [84] introduced a "directionality factor" in the regenerator porous zone to model a membrane used to block the DC flow in the experimental setup of a thermoacoustic engine. This additional viscous resistance, when the working fluid moves from the cold to the hot heat exchanger, was tuned to obtain a net-zero mass flow rate. Likewise, Liu et al. [85] modeled an elastic membrane eliminating the DC flow in the looped system by exploiting the "Fan Model" in the Fluent software package. Scalo et al. [69] clearly showed that, without any counter pressure drop to block the Gedeon streaming, the overall thermoacoustic efficiency is about 10%. Yang et al. [86] instead performed a numerical parametric analysis, by varying the Reynolds, Keulegan–Carpenter (KC) and Womersley numbers, to study the effectiveness of a short tube in producing an opposite pressure drop for the same purpose. Yu et al. [85] distinctly illustrated a comparison in terms of the mean time–temperature profile along the coordinate of the traveling-wave device with and without such a deliberate "minor loss", showing that the temperature difference along the regenerator decreased from 600 K to 300 K (and also, as a consequence, the efficiency reduced sharply).

Furthermore, considering the high impact of a good design of such components on the performance, many works in the literature have studied, from a microscopic point of view, the so-called "jet pump", a geometry inducing an asymmetric concentrated pressure drop. A 3D sketch of a jet-pump is illustrated in Figure 9. Backhaus and Swift [87] introduced the expression for calculating this pressure drop, in a quasi-steady-state approximation, as a function of the contraction/expansion coefficients and the ratio between the maximum and minimum areas of the jet pump. Boluriaan and Morris [88] presented numerical results of the net pressure drop generated by a sole jet pump or by an orifice. As the latter geometries were not optimized, the mass flow rate was not canceled. Later, Oosterhuis et al. [89] carried out numerical simulations on a jet pump of different geometries hit by a traveling wave promoted by an impedance boundary condition at the ends of the domain. By making the acoustic displacement dimensionless, four different flow regimes were identified in relation to the Keylegan–Carpenter (KC) numbers based on the diameter and length of the jet pump configuration. According to these results, the steady-state solution is valid only for a small range of KC_D (small amplitude). The last finding is contradictory to what was found by Swift et al. [8] regarding the prediction of the minor losses with steady-state correlations. In subsequent work, Timmer et al. [90] showed the crucial role of flow separation in the jet pump performance by varying the geometry of the jet pump, pointing out the decrease in the pressure drop available to contrast the Gedeon streaming and the opposite increase in acoustic power dissipation. Oosterhuis et al. [91] ran some experiments to investigate the influence of turbulence on the jet pump performance. Specifically, turbulent flows identified by the criteria in [92] can lead to a reduction in the flow separation in the diverging part of the jet pump, and this can therefore boost performance. The experimental results in the laminar regime were also compared with previous numerical results [91].

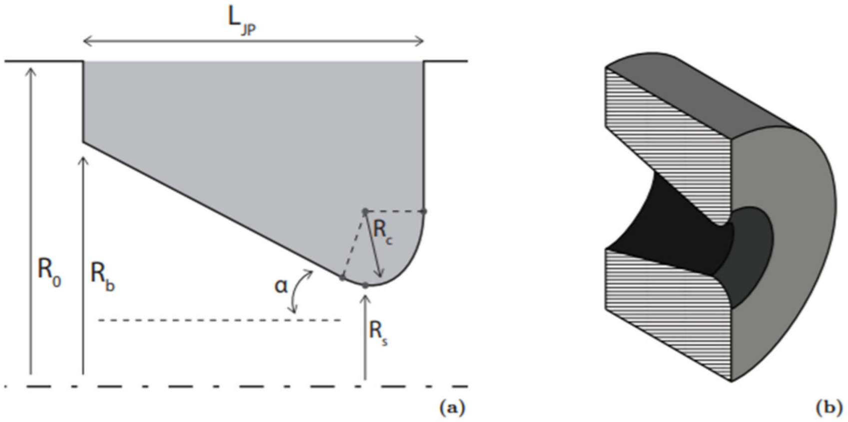

Figure 9. (**a**,**b**) Jet pump [91].

4. CFD-Based Models

Two models can be typically found in the available literature, based on the control volume considered: the first one concerns the so-called "thermoacoustic core" (TAC), a single unitary cell representing the stack or the heat exchangers (HXs), and the second one simulates a full thermoacoustic device with microscopic and macroscopic approaches for the TAC. It should be noted that the nomenclature "microscopic"/"macroscopic" comes from the available literature in porous media. Microscopic refers to "high-fidelity models", in which the geometry is modeled in detail in the computational domain, while a macroscopic model is built using the volumetric average of the high-fidelity equations on a representative elementary volume (REV). Simulations of single TACs, at the microscopic level, can be used to increase the performance of these devices, by varying the stack geometrical parameters (spacing, length, thickness), HX parameters (spacing, length, thickness), working fluid or operating pressure amplitude level, described by the drive ratio Dr (ratio between the pressure amplitude and average pressure). Models of full thermoacoustic devices are needed to evaluate the performance of the system, energy conversion efficiency for engines or the coefficient of performance (COP) and cooling temperature in refrigerators [93]. A summary scheme of the criteria, used to classify and analyze these 2D or 3D models in the time domain with a CFD approach, is presented in Figure 10.

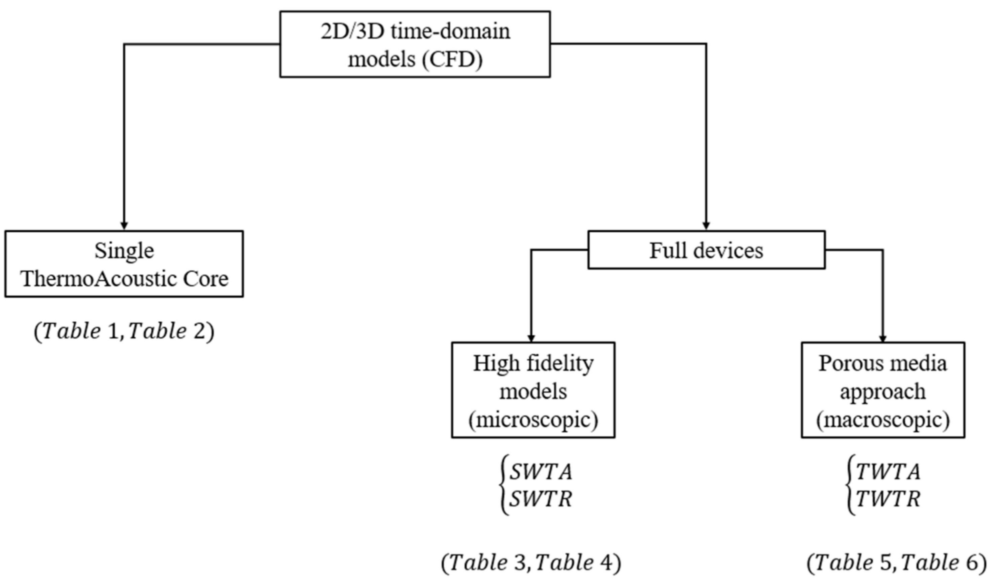

Figure 10. Criteria used to classify and analyze 2D/3D CFD models.

4.1. Single TAC

The computational domains of a TAC simulation have almost always been extracted from 2D standing-wave device models equipped with a parallel-plate stack configuration (and HXs eventually), to exploit the geometrical periodicity. While the total longitudinal size of the device has to be taken into account in the computational domain of an engine TAC (the frequency and amplitude of pressure and velocity oscillations significantly depend on this size), for refrigerators, a reduction in the size of the computational domain has often been adopted in CFD-based simulations. However, in order to avoid the pressure and velocity distributions being affected by a domain reduction, Mergen et al. discovered that a resonator length which is 10–20% of the acoustic wavelength is needed to simulate a smaller domain without compromising the accuracy of the solution [94]. Stacks, as well as heat exchangers, are modeled considering a zero or finite thickness. In case a zero thickness is considered for the fluid dynamics simulation, a 1D energy conservation equation has to be solved for the solid, coupled to the fluid thermal field, to account for the thickness of the plates, as proposed by Marx and Benon [95]. In this case, the effects of the actual plate on the velocity field, such as the vortices resulting from the edge of the stack [96], are not considered.

The mesh used for these simulations must be a fraction of the minimum between the viscous and thermal penetration depths, to correctly evaluate the gradients of the variables near the walls:

$$\delta_v = \sqrt{\frac{2\nu}{\omega}},\ \delta_k = \sqrt{\frac{2\alpha}{\omega}} \tag{4}$$

Marx and Benon [97] demonstrated that for a standing-wave TAC, the computational cost, calculated as the product of elements in the x, y direction and the number of time steps, is inversely proportional to the square root of the frequency. As a consequence, for their simulations, they chose a frequency of 20 kHz, which does not impact the results, although this value is used in real-life applications.

To model thermoacoustic refrigerators, an equivalent acoustic boundary condition has to be used to promote the inlet/outlet (acoustic) work flux. The simplest is a harmonic pressure or velocity boundary condition [96,98]. Another method, more expensive in terms of computational costs, is the use of a dynamic mesh with a prescribed reciprocating velocity to simulate the membrane displacement of a speaker or a piston [99]. Namdar et al. [100] highlighted that, for a specific hot–cold temperature difference, the right choice of the drive ratio as input is needed to allow the HXs to work correctly according to their thermodynamic role and therefore guarantee a positive coefficient of performance (COP). At a periodic steady state, from an energy point of view, the difference between the work fluxes which enter or leave the computational domain through one of the above boundary conditions must be balanced by the difference between the heat exchanged by hot and cold HXs. When the heat exchangers are not present, the stack ends play the role of a proper HX because they exchange a nonzero time-averaged heat flux with the fluid, as emphasized for the first time by Cao et al. [101]. Later, Ishikawa et al. [102] also found that, at the middle of the stack, there is no net average heat transfer time, over a period, between the fluid and the solid isothermal surface, which instead occurs at a distance close to the peak–peak air particle displacement. These phenomena cannot be captured by linear thermoacoustic theory which intrinsically neglects the end effects. While an isothermal boundary condition has always been applied on HX surfaces, considered as an isothermal energy tank, for the fluid–solid interface of the stack, several choices are possible, depending on the thermal capacity of the materials involved. In general, a conjugate heat transfer approach can be used [96], with the continuity of the heat flux and temperature at the fluid–solid interface, when the final aim of the simulations is to evaluate the temperature difference that develops at the ends of the stack under oscillating conditions. If this is not the case, thermal boundary conditions, with a constant assigned temperature gradient, can be adopted when the solid thermal capacity is much higher than that of the fluid [19].

In some cases, numerical analyses of TACs have been used to consolidate design choices already reached with LTT such as gaps between plates, the length, the thickness, the position and the material properties of both the stack and HX. For instance, the plate length should be much smaller than the acoustic wavelength, placed at the middle between the pressure and velocity antinodes to guarantee the maximum cooling effect [93]. Furthermore, an anisotropic thermal conductivity, which is higher in the direction of its width and lower in the axial direction, allows promoting an oscillating heat transfer with the fluid and to sustain the mean temperature gradient in the transversal and longitudinal directions [103]. Finally, the distance between the plates should be of the same order of magnitude as the thermal penetration depth δ_k [103].

Verification of CFD results with linear theory in terms of the velocity profile along the channel [97], the temperature difference across the stack [104] and the pressure/velocity distribution confirms that the best agreement between these data is obtained for low values of the drive ratio. However, it should be mentioned that the results obtained from a 3D model of a square-section TAC [105] illustrate disagreement with all other 2D parallel plate simulations because the comparison with linear theory, in terms of the temperature difference along the stack, fits better at high- rather than low-amplitude regimes, as it would be expected based on the previous 2D results. Moreover, CFD-based works corroborated that the optimal length of the HXs is almost equal to the peak–peak air particle displacement [97,106]. Marx and Benon [97] also suggested that there is an optimal gap between the stack and HXs to maximize the COP of a refrigeration system.

The CFD approach, as shown by comparison with experimental data [96,107], can capture nonlinear losses, including thermal wave distortion [48], and minor losses [108], which can strongly affect the performance of the devices [109]. Hamilton et al. [110] investigated the harmonics and shock waves in the resonator of an engine TAC and showed how they can be mitigated by using variable cross-section resonators. For the first time, Migliorino and Scalo [108] adopted carbon dioxide in transitional conditions as a working fluid, to try to obtain a better engine performance. The results showed that with transitional fluids, the potential suitable work is higher, but they also require a higher heat input. It is therefore not obvious that the thermoacoustic efficiency improves. An engine is said to be "unloaded" if the whole mechanical energy converted from the heat exchanged due to the temperature gradient is dissipated by nonlinear losses along the resonator. The engine is said to be "loaded" if a specific boundary condition capable of describing an electric load absorbing the acoustic power produced by the stack is implemented in the overall model. Moreover, the model recently built by Ja'fari et al. [111] is an unloaded engine equipped with a single plate of the stack and HXs, aimed at studying the Rayleigh streaming inside the stack at a high amplitude. Boroujerdi and Ziabasharhagh [107] developed a loaded thermoacoustic engine with an acoustic load, by mixing LTT, adopted far away from the stack, and the CFD approach for the thermoacoustic core. Finally, to the authors' knowledge, Sharify et al. [112] are the only authors who developed a model for a TAC of a traveling-wave engine. In particular, they isolated the core from a looped tube, including four regenerator plates and two HX plates, and implemented an acoustic impedance boundary condition at the left and right ends of the domain.

Tables 1 and 2 present a sketch of the domain, geometrical characteristics, boundary conditions and software employed for the simulations of single TACs in the available literature. Specifically, for the TAC of thermoacoustic refrigerators, Table 2 shows the main parameters that affect the results of the simulations, listed with the values used by the different authors, such as the working fluid, solid, porosity ϕ, dimensionless plate spacing y_0/δ_k, stack length L_s/λ, position $k_w x_s$, drive ratio and type of oscillating boundary condition and thermal boundary condition at the fluid–solid interface. From the numerical values reported in Table 2, it can be seen that the porosity adopted in the numerical simulations is never less than 0.5, because even minor losses related to the abrupt geometrical discontinuities between the stack plate and the free fluid region would negatively affect the performance. Similarly, dimensionless stack spacing values (y_0/δ_k) have always been considered in the range 0.7–3.3. It has to be said that the optimal theoretical value to maximize the thermoacoustic effect for a standing-wave device made of a parallel-plate stack is about 1.1 [16]. Stack lengths never exceed a twentieth of the wavelength, while most stack positions are found to be equal to $3\pi/4 \approx 2.35$, between the pressure antinode and velocity node. For the TAC of thermoacoustic engines, specified in the last rows of Table 2, the working fluid, porosity and temperature difference at the ends of the stack are reported because the other parameters theoretically depend on the frequency.

Table 1. Model and computational domain of the single TACs found in the literature (in blue, green and red are a cold HX, a stack and a hot HX, respectively); the wave symbol is the oscillating boundary condition. In the second column, it is specified if the model is 3D or 2D axisymmetric.

N°	Model	Typical Computational Domain at the Microscopic Scale of the TAC	Refs.
I	SWTAR		[96] [104]
II	SWTAR	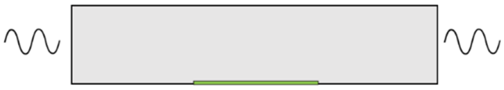	[101]
III	SWTAR		[106]
IV	SWTAR		[48] [95] [102]
V	SWTAR	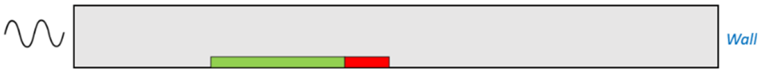	[103]
VI	SWTAR	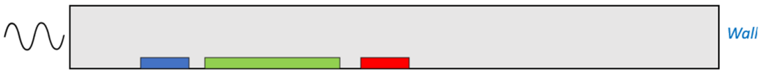	[97] [93]
VII	SWTAR with square stack (3D)	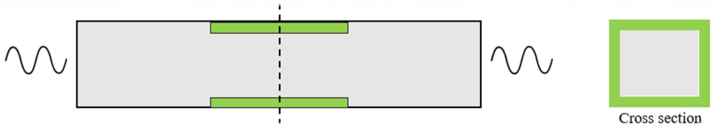	[105]
VIII	SWTAR (SWTAE)	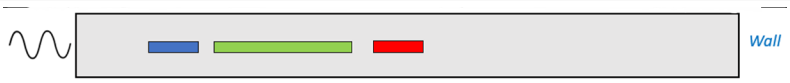	[100] [111]
IX	SWTAE		[108] [110]
X	SWTAE		[107]
XI	SWTAE	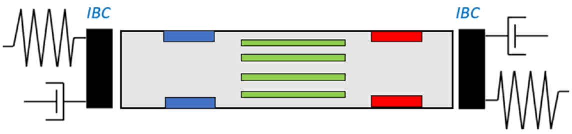	[112]

Table 2. Detailed characteristics of simulations of single TACs.

Refs.	Fluid	Solid	ϕ	y_0/δ_k	$k_w x_s$	Dr (%)	L_{stack}/λ	Oscillating BC	Fluid–Solid Interface BC	Software
[96]	Helium	Steel + fiberglass	0.85	-	2.35 ÷ 3	0.28 ÷ 2	1/400	Vorticity	Coupled	Proprietary
[101]	-	-	1	0.83 ÷ 3.3	0.23–0.63	1.4 ÷ 7	0.024	Velocity	Isothermal	Proprietary
[106]	Helium	Steel + fiberglass	0.66	3.5	2.35	1.5–2.5	0.0195	Velocity	Coupled	Proprietary
[102]	Air	-	1	0.33–3.33	0.785	1.7–8.5	0.0023–0.05	Pressure/velocity and temperature	Isothermal	PHOENICS
[95]	Air	Mylar	1	1.9	1.5 ÷ 3.25	0.7 ÷ 11.2	0.0088	Pressure	1D solid energy equation	Proprietary
[48]	Air	-	1	2.5	2.13	0.7 ÷ 11.2	1/40	Pressure	Isothermal	Proprietary
[103]	Air, Argon	Theoretical solid	0.57 ÷ 0.83	1.4–2.4	0.15 ÷ 0.7	≤16	0.038 ÷ 0.007	Velocity	Coupled	Proprietary
[97]	Air	Mylar	1	0.69 ÷ 2.7	2.13 ÷ 2.7	0.8 ÷ 16.8	1/40–1/20	Pressure	Isothermal or 1D solid energy equation	Proprietary
[93]	Helium	Kapton, steel, glass, copper	0.88 ÷ 0.97	0.63 ÷ 3.3	2.35	0.05 ÷ 1.7	0.009 ÷ 0.068	Pressure/velocity and temperature	Coupled	Comsol Multiphysics
[105]	Helium	Cordierite	0.787	-	0.51	1.7–8.5	-	Velocity	Coupled	Ansys Fluent
[100]	Air	-	0.8	2.5	2.41	1	0.04	Pressure	Coupled	OpenFOAM
[104]	Air	Glass	0.87	2.6	0.785	0.7	0.014	Pressure/velocity and temperature	Coupled	STAR-CD
[108]	CO_2	-	0.5			engine			$\Delta T \leq 200$ K	Proprietary
[107]	Helium	Stainless steel	-			engine			Coupled	Proprietary

Table 2. *Cont.*

Refs.	**Fluid**	**Solid**	ϕ	y_0/δ_k	$k_w x_s$	**Dr (%)**	L_{stack}/λ	**Oscillating BC**	**Fluid–Solid Interface BC**	**Software**
[112]	Air	-	0.75			engine			$\Delta T = 210$ K	Proprietary
[110]	Air	-	1			engine			$T_{hot}/T_{cold} = 2.6$	Proprietary
[97]	Air	-	0.8			engine			$\Delta T = 300$ °C	OpenFOAM

4.2. Full Device Models

Despite the lower computational costs of simulating a single TAC, in order to capture the overall performance of a system, solutions computed on the reduced domains may not always be satisfying. In fact, Rogosinzky et al. [113] noticed that the pressure field can depend on the number of fluid channels involved in the computational domain. This finding was confirmed by Nowak et al. [114], who discovered that simulations of a single TAC overestimate the pressure amplitude as the impact of additional losses coming from other TACs is neglected.

In the following two sections, firstly, full devices, solved with a CFD-based approach at the microscopic scale, will be presented, followed by models that use a macroscopic approach for porous media that describe the single TAC. In fact, solutions at the microscopic scale are not always convenient, both for the prohibitive computational costs and for the random structures of regenerators. Simulations involving components described with a macroscopic approach (HXs and/or the stack/regenerator) will be presented after briefly reviewing the porous media sub-models that are generally adopted. Finally, some numerical aspects emerging from the CFD simulations (mesh and time step, initial conditions, numerical schemes and algorithm) will be discussed.

4.2.1. Microscopic Models

At the microscopic level, a full standing-wave device consists of different TACs in the transversal direction and the full length in the longitudinal direction. The computational domain of a complete device consists of a longitudinal length equal to a half or a quarter wavelength, and a diameter/section able to contain all plates that compose a stack. Generally, a basic standing-wave device presents a thermal buffer tube, close to the hot side of the stack, the stack itself and the rest of the resonator.

Zink et al. investigated how a 90° bend affects the limit cycle of an unloaded standing-wave thermoacoustic engine and concluded that the pressure level lowers the performance of the device, compared to the straight model, as well as in stationary flows where each curvature causes a local pressure drop [115,116]. In a subsequent work, Zink et al. [117] replicated the above model by adding a secondary stack, working as a cooling stack, driven by the pressure oscillation generated by the first one, showing that a temperature lower than the ambient one can be reached on one side of the second stack. Skaria et al. [118] performed comparisons between CFD, DeltaEC and experimental results for a twin standing-wave thermoacoustic engine (coupling of the identical and mirrored standing-wave engines) and a thermoacoustically driven standing-wave thermoacoustic refrigerator, showing that CFD-based results better agree with experimental data. A similar setup, with a secondary cooling stack, was also investigated by Ali et al. [119], who performed a sensitivity analysis on the temperature difference produced in the secondary stack by six different working fluids. Bouramdane et al. [120] investigated different corrugated stack geometries with a fixed temperature gradient along the primary stack, concluding that for a TAE, a corrugated surface allows increasing the acoustic power, while for a TAR, the maximum temperature gradient is achieved with a flat parallel-plate stack. Chen et al. [121] studied the synchronization of a similar double thermoacoustic engine, by introducing a large air box in the model. Rogoziński [122], instead, reproduced a dual standing-wave device, in which the two units were connected by a reciprocating piston modeled with a dynamic mesh. The basic model of the standing-wave device was later reproduced in other articles [123,124]. In the first article, it was shown that the presence of a secondary stack affects the pressure distribution inside the resonator, while in the second article, the parametric results from varying the stack and resonator lengths were compared to LTT. Kuzuu and Hasegawa introduced HXs in their setup and quantitatively analyzed the impact of nonlinear thermal effects on the heat exchanged in the cold and hot HXs, finding a difference of about ten percent from the DeltaEC results [125,126]. Geng et al. performed high-fidelity 3D simulations with the LES turbulence model in order to investigate nonlinear effects such as minor losses and mass streaming [74,127]. Likewise, Guo et al. [76] compared the overall performance of the above standing-wave engine driven by waste heat and a cryogenic liquid with equal temperature differences. Another 3D model was developed by Gupta et al. [128] by adopting a longitudinal pin-array stack, helium as a working fluid and a k-ϵ turbulence model. Zhang et al. [129] evaluated the thermoacoustic efficiency of the stack versus different prescribed distributions of the solid temperature along the stack, concluding that the higher the mean temperature, the higher the heat input, acoustic power and efficiency. The work of Harikumar et al. [130] focused on a thermoacoustic system within a looped tube modeled from a microscopic point of view, equipped with a parallel-plate solid stack thermally coupled with the working fluid. They particularly analyzed the flow structures generated near the edge plates, showing a good agreement with experimental data.

For the first time, Lin et al. [70] realized a high-fidelity model of a standing-wave thermoacoustic piezoelectric engine. More specifically, a piezoelectric diaphragm was considered by introducing a multi-oscillator broadband time-domain impedance boundary condition (MOB-TDIBC) instead of a rigid wall, on the right side of the computational domain, to simulate a deformable membrane absorbing the acoustic work "produced" by the engine. Switching from the frequency domain to the time domain is not trivial because physical admissibility, as well as numerical stability, should be ensured. The multi-oscillatory fit of the impendence was demonstrated to be more accurate than the single-frequency impedance. Imposing an impedance boundary condition means, after a procedure involving numerical resolution of convolution integrals, prescribing the wall-normal velocity and fluctuation pressure. The data needed for this boundary condition implementation were provided by experiments. A simpler impedance boundary condition was directly derived from linear theory in [131] and implemented in COMSOL Multiphysics to replace the effect of a liquid column in a U-shaped tube (aimed at enhancing the thermoacoustic instability). Similarly, for a thermoacoustic refrigerator, a boundary condition, involving the electromechanical coupling in the thermoacoustic refrigerator, was adopted by Tisovsky et al. [132] to allow the mesh to move with a prescribed velocity profile.

Table 3 presents all the possible sketches of full thermoacoustic devices entirely modeled at the microscopic scale. Table 4, in addition to the main geometrical characteristics, summarizes the temperature difference applied along the stack, and the amplitude/frequency of the periodic pressure oscillation due to the thermoacoustic instability.

Table 3. Model and computational domain of full device simulations at the microscopic scale. In the second column, it is specified if the model is 3D or 2D axisymmetric.

N°	Model	Typical Computational Domain at the Microscopic Scale	Refs.
I	Basic SWTAE, $\frac{\lambda}{4}$ $\left(\frac{\lambda}{2}\right.$		[58] [115] [116] [124] [129]
II	Refrigerator driven b	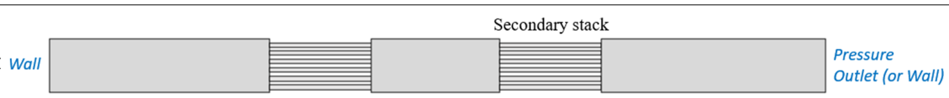	[117] [118] [123]
III	Piezoeletric SWTAE, (2D axysymmetric)	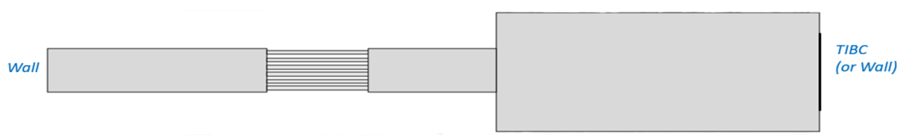	[70]

Table 3. *Cont.*

N°	Model	Typical Computational Domain at the Microscopic Scale	Refs.
IV	Dual SWTAE		[118] [121]
V	Dual SWTAE with piston	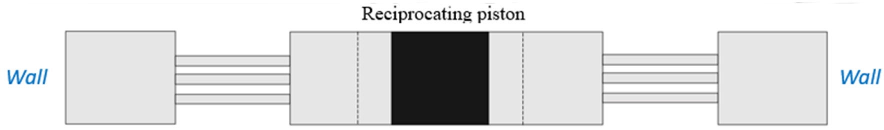	[122]
VI	3D SWTAE, with parallel-plate stack		[74] [76] [127]
VII	3D SWTA, with longitudinal pin-array stack		[128]
VIII	SWTA with HXs, $\frac{\lambda}{4}$	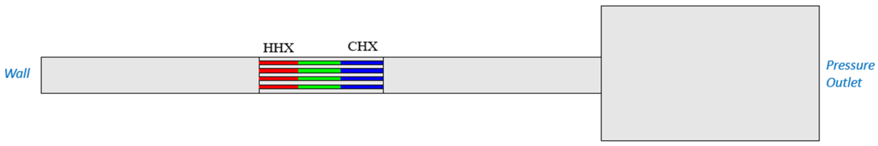	[125] [126]
IX	Looped tube + resonator		[130]
X	SWTAR	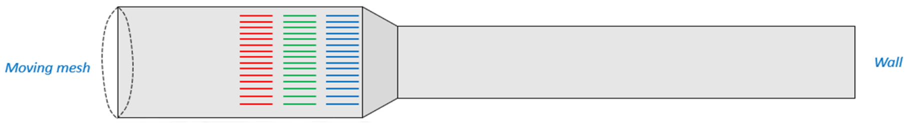	[132]
XI	SWTAE	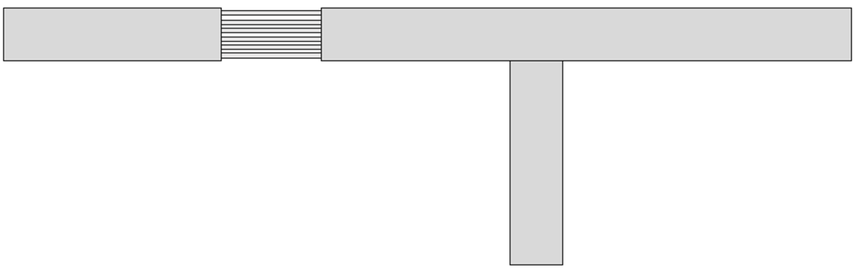	[133]

Table 4. Detailed characteristics of full device simulations at the microscopic scale.

Refs.	Fluid	ϕ	$y_0(or\ r_h)$	x_s	L_{stack}+L_{hx}	L_{tot}	Fluid–Solid Interface BC	Frequency [Hz]	Turbulence	Pressure Amp.(or ΔT)	Software
[115]	Air	-	0.25 mm	-	10 mm	150 mm	$\Delta T = 400$ K, $h_c =$ 50 W/m^{2}K	600	$k-\epsilon$	5125 Pa	Ansys Fluent
[116]	Air		0.25 mm	30 mm	10 mm	150 mm	$\Delta T = 400$ K, $h_c =$ 50 W/m^{2}K	614–629	$k-\epsilon$	8584–7625 Pa	Ansys Fluent
[124]	Air-N_2-Ar	0.375	0.15 mm	80 mm	50–70 mm	0.33–0.45 m	$\Delta T = 440$ °K	217–307	$k-\epsilon$	-	Ansys Fluent
[129]	Air	-	1.5 mm	1 m	90 mm	3 m	$\Delta T = 125$ K	$20-21$	ILES	$432-694$ Pa	Comsol-Multip.
[58]	Air	0.5	0.5 mm	0.1 m	30 mm	0.5 m	$\Delta T \leq 250$ K	$178-181$	$k-\epsilon, \omega,\ lam.$	≤ 7200 Pa	Ansys Fluent
[117]	[115] I stack		0.25 mm	45 mm	5 mm	150 mm	$h_c =$ 50 W/m^{2}K	614	$k-\epsilon$	≈ 3 K	Ansys Fluent
[118]	He, Ar, N_2	-	-	-	51 mm	-	$\Delta T = 700$ K	25–125	$k-\epsilon$	$\leq 20{,}000$ Pa	Ansys Fluent
[123]		0.5	0.25 mm		as [115,117]		$\Delta T = 600$ K	≈600	-	2325 Pa (≈ 1.5 K)	Comsol-Multip.
[70]	Air	0.3–0.6	0.3–0.65 mm	60 mm	37.5 mm	0.510 m	$\Delta T \leq 490$ K	382–391	Laminar	≤ 6500 (unloaded)$\leq$ 4700 (loaded)	Proprietary
[121]	Air	0.5	0.5 mm	0.1 m	30 mm	variable	$\Delta T = 600$ K	230–420	$k-\epsilon$	$4000-6000$ Pa	Ansys Fluent
[122]	-	0.5	0.25 mm	30 mm	10 mm	150 mm $\cdot$ 2	$\Delta T = 400$ K	140–350	$k-\epsilon$	-	Ansys Fluent
[72,127]	Air	0.5	0.25 mm	0.1 m	30 mm	0.5 m	$\Delta T \leq 700$ K	$178-181$	LES	≤ 9000 Pa	Ansys Fluent
[128]	He	0.91	0.175 mm	0.1 m	0.1 m	1.2 m	$\Delta T = 400$ K	200	$k-\epsilon$	420,000 Pa	Ansys Fluent
[125,126]	Air	0.5	3 mm	1 m	90 mm	4.59 m	$\Delta T = 120$ K	$20-21$	Laminar	≤ 1000 Pa	LS-FLOW
[130]	Air	0.625	0.25	0.55 m	100 mm	1.6 m	$\Delta T = 0$	45, 120	SST $k-\omega$	1480 Pa, input	Ansys Fluent
[132]	Air	1	-	20 mm	85 mm	861 mm	Thermal baffles with prescribed heat flux	500	-	$120{,}000$ Pa	OpenFOAM

4.2.2. Macroscopic Models

Stack and heat exchangers can be described using a macroscopic approach, when modeling a whole thermoacoustic device, in order to reduce computational costs and make the simulation of an actual device affordable. The macroscopic equations that can be used to describe heat and mass transfer through a porous medium are derived from volume averaging the NSEs [25]. In order to be mathematically closed, models of the interaction between the fluid and solid matrix of the porous media are needed both for the momentum and energy equations. For the momentum equations, the Darcy, Forchheimer or generalized models are available [134,135]. For the energy equations, two main models exist for porous media, the local thermal and local non-thermal equilibrium (LTE and LTNE) [136].

Most steady-state porous media correlations express the pressure drop as the sum of a linear term with velocity (Darcy, viscous term) and a nonlinear one scaling with the velocity squared (Forchheimer or inertial term). Even if these models are strictly derived and applied only for stationary flows, they are fairly accurate when the oscillation frequency tends to zero or the hydraulic radius r_h is much smaller than the viscous penetration depth δ_v. This is acceptable especially when the frequency oscillation tends to zero or the hydraulic radius r_h is much smaller than the viscous penetration depth δ_v, which is generally verified in a traveling-wave device.

Although there are two different formulations of porous media correlations, according to the type of averaging used for the NSEs (superficial formulation (SF) when phase averaging is performed; physical formulation (PF) when intrinsic averaging is performed [134]) or the input parameters used to implement the porous media source terms, the physical foundation on which they are based is the same. These parameters can be the permeability β $\left(\mathrm{m}^2\right)$ and inertial factor C_2 $\left(\mathrm{m}^{-1}\right)$, the dimensionless skin friction C_{sf} and form drag C_{fd} coefficients (uniquely linked to β, C_2, respectively) or the hydraulic radius r_h (or wire diameter d_w) and porosity ϕ.

$$\boldsymbol{S} = -\frac{\mu}{\beta}\boldsymbol{v} - \frac{1}{2}C\rho_f\boldsymbol{v}|\boldsymbol{v}| \tag{5}$$

$$\boldsymbol{S} = -f_{factor}\frac{\rho\boldsymbol{v}|\boldsymbol{v}|}{4d_w},\ f_{factor} = C_{sf} + \frac{C_{fd}}{Re},\ Re = \frac{\phi}{1-\phi}\frac{d_w u}{\nu} \tag{6}$$

$$\boldsymbol{S} = -\left(\frac{\mu}{\beta} + \frac{F_\varepsilon}{\sqrt{\beta}}|V|\right)V,\ \beta = \frac{d_w^2\varepsilon^3}{150(1-\varepsilon)^2}F_\varepsilon = \frac{1.75}{\sqrt{150\varepsilon^3}} \tag{7}$$

By comparing the pressure drop expressed in terms of permeability β and inertial C and that expressed in terms of the dimensionless parameters C_{sf} and C_{fd},

$$C_{sf} = \frac{1}{\beta}4d_w^2\frac{\phi^2}{1-\phi},\ C_{fd} = 2d_w C\phi^2,\ C = \frac{2F_\varepsilon}{\sqrt{\beta}} \tag{8}$$

The porous media heat transfer model for thermoacoustic applications is crucial because it can determine the success or the failure of a CFD simulation of a standing-wave device. The model built by Oumayama et al. [137] is one example of a stack refrigerator treated as a homogenous porous medium with a Darcy–Forchheimer model coupled to a thermal equilibrium model. To the authors' best knowledge, successful CFD models of a standing-wave thermoacoustic engine based on a macroscopic scale have not been found in the available literature. In this regard, Guoayo et al. [138] tried to macroscopically model the parallel-plate stack and HXs of an unloaded standing-wave thermoacoustic engine in Ansys Fluent, using the available LTE approach. In this case, the model was not able to predict the engine startup, because the principle of operation of a standing-wave engine is based on the irreversible heat exchanged between the fluid and solid matrix in the stack. A macroscopic approach was instead adopted to model the HXs, as well as in other papers [131,139]. In the first paper, the use of a stack with decreasing section area allowed maintaining the ratio y_0/δ_k close to the optimal value along the longitudinal coordinate, while in the second paper, an analysis of the higher harmonics and nonlinear hydrodynamic losses was conducted. On the other hand, there are numerous models of traveling-wave engines and refrigerators adopting the LTE, LNTE or hybrid approaches. In the latter, when the solid thermal capacity is much higher than the fluid capacity, a single fluid energy equation may be considered, with a source term describing the heat transfer process:

$$S_h = -\alpha_T(T - T_s) \tag{9}$$

where T_s is the temperature of the solid matrix and T is the fluid temperature. Scalo et al. [69] proposed the following expressions for α_T:

$$\alpha_T = \alpha_h \frac{\rho R}{\gamma - 1},\ \alpha_h = \frac{1}{\tau_h},\ \tau_h = \frac{r_h^2}{\alpha} \tag{10}$$

which can be re-arranged by invoking the relation between the constant gas, R, and the specific heat as follows:

$$\alpha_T = \frac{k}{r_h^2}\frac{1}{\gamma} \tag{11}$$

For a pure LTE approach, instead, only the equivalent specific heat and thermal conductivity have to be specified.

$$k_{eq} = \phi k_f + (1-\phi)k_s,\ \left(\rho C_p\right)_{eq} = \rho C_p \phi + (1-\phi)\rho_s C_s \tag{12}$$

For a pure LNTE approach, the source terms can be modeled in the fluid and solid energy with the following expressions [140]:

$$\begin{gathered} S_h = \frac{h_p A\left(T_s - T_f\right)}{\phi},\ S_{h,s} = -\frac{h_p A\left(T_s - T_f\right)}{1-\phi} \\ h_p = \frac{0.33 k_f}{4 r_h}\left(\frac{\frac{8\rho_f r_h}{\mu} V_p \rho_r}{A_{sp}\phi}\right)^{0.67} \end{gathered} \tag{13}$$

where A_{sp} and V_p are the total interfacial surface and volume of the porous zone. An initial example of a non-equilibrium porous medium model in oscillating flows, for a Stirling Engine regenerator, was developed by Tew et al. [141], who defined an equivalent thermal conductivity that includes the stagnant one, together with tortuosity and dispersion effects.

Lycklama à Nijeholt et al. [142] presented one of the first models of a traveling-wave engine with a CFD approach, using the momentum source terms expressed in Equation (6) and the energy source term expressed in Equation (9) in a 2D axisymmetric model. The core was placed in a double-Helmholtz resonator, more specifically in a concentrical tube on the right side of the system. The annular gap between the tube and the resonator serves as a feedback inertance connected to the compliance at the right side of the engine, as sketched in the first row of Table 5. Nonlinear and multidimensional phenomena, such as vortices by the jet coming out of the feedback inertance (leading to a 2D temperature field in the hot buffer), and the Gedeon streaming caused by a time-averaged pressure drop along the regenerator, were observed. However, the simulation was stopped before reaching the limit cycle. Yu et al. [85] worked on a similar setup including a secondary ambient HX which allowed reaching the limit cycle. Unlike the previous work, they adopted an LTE model. This means that, in contrast to the above-mentioned standing-wave engine devices, the startup process of a traveling-wave model is not sensitive to the specific thermal approach adopted. From a modeling point of view, the authors proposed a very effective method to cancel the Gedeon streaming, introducing a fan model able to produce a pressure difference Δp, opposite to that developed due to the pressure drop along the regenerator. The validation with experimental data was carried out in terms of the pressure amplitude and the onset of the thermoacoustic phenomena, showing a satisfying agreement. Scalo et al. also [69] carried out 3D high-fidelity numerical simulations of the same traveling-wave engine and calculated its overall efficiency. Lycklama à Nijeholt et al. [84] later realized a 2D and 3D torus-shaped traveling-wave engine closer to reality compared to the previous model, whose geometry cannot be constructed practically. Furthermore, they introduced an "asymmetric factor" to remove the Gedeon streaming and a purely inertial resistance in a specific porous zone of the resonator to simulate the acoustic load. A similar torus configuration was also modeled by Ali et al. employing a thermal equilibrium model [72]. For the first time, Liu et al. [143] built a CFD-based model of a multi-stage traveling-wave engine with the same LTE approach. The actual closed-loop geometry was "unrolled" in a straight pipe for which periodic boundary conditions were considered at the boundary surfaces, as depicted in the third sketch of Table 5. The torus-shaped device or its rectified version is not the only way to develop the correct phase between the pressure and velocity. A thermoacoustic orifice pulse tube refrigerator (TOPTR) is considered a traveling-wave device, and one was simulated by Antao and Farouk [144–146]. Their 2D axisymmetric simulations relied on a Darcy–Forchheimer model of both a regenerator and HXs and showed the importance of an LNTE approach and the wall thickness in the various components to accurately evaluate the transient cooling temperature. Moreover, they underlined that, at the optimum frequency, the presence of a couple of counter-rotating vortices can enhance the performance of the TOPTR, while at different frequencies, the same nonlinear effect leads to a performance reduction [144,145]. For the same system, the authors also showed an improvement in the performance by varying the taper angle of the pulse tube and the diameter of the hot HX because the streaming velocity was reduced [146]. In Tables 5 and 6 sketches of the computational domains and detailed characteristics of the macroscopic models employed for the thermoacoustic core are presented respectively.

Table 5. Model and computational domain of full device simulations at the macroscopic scale. In the second column, it is specified if the model is 3D or 2D axisymmetric.

N°	Model	Typical Computational Domain at the Macroscopic Scale	Refs.
I	Theoretical TWTAE (3D)	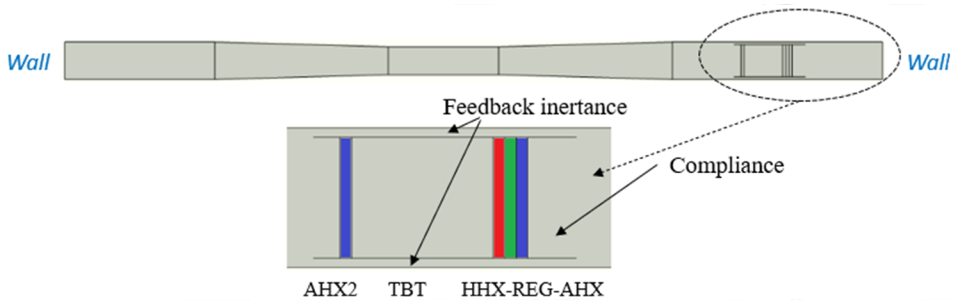	[69] [85] [86] [142]
II	Looped tube + resonator TWTAE	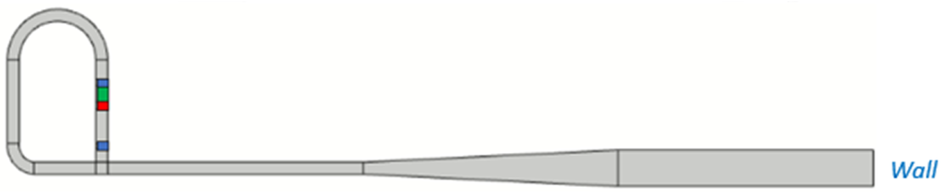	[72] [84]
III	1 of the 3 stages of a TWTAE (unrolled) (2D axysymmetric)	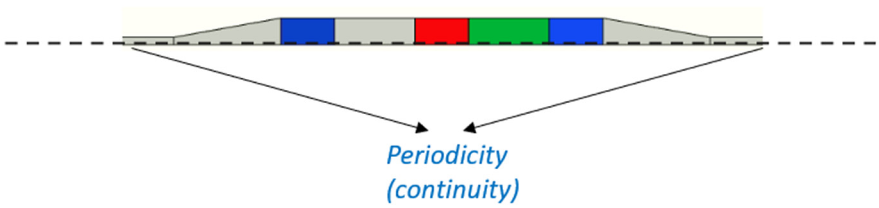	[143]

Table 5. *Cont.*

N°	Model	Typical Computational Domain at the Macroscopic Scale	Refs.
IV	TAOPTR (2D axysymmetric)	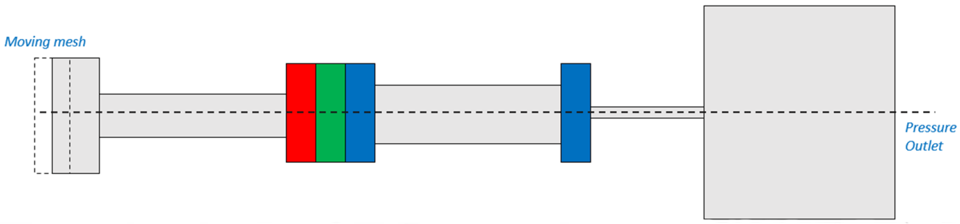	[144] [145] [146]
V	SWTAE	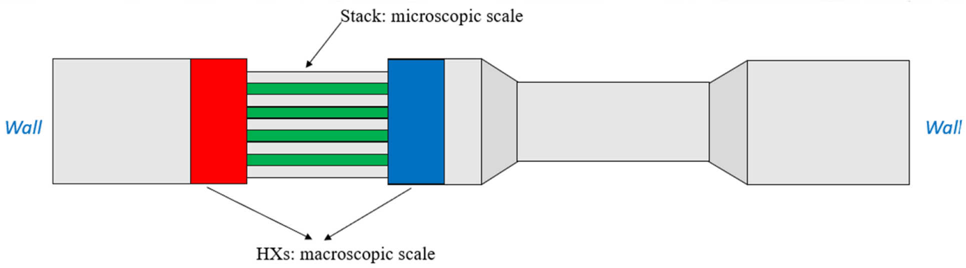	[131] [138] [139]
VI	SWTAR	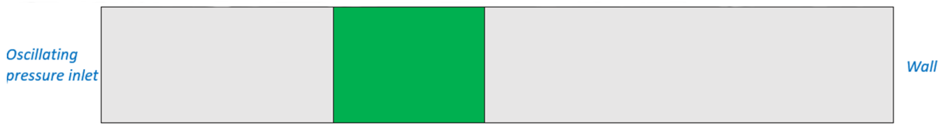	[137]

Table 6. Detailed characteristics of full device simulations at the macroscopic scale.

Refs.	Fluid	Stack/Regenerator		HX		Frequency [Hz]	Turbulence	Pressure Amp. (or Tcooling/ΔT)	Software
		Momentum	Energy	Momentum	Energy				
[142]	Air	Darcy–Forchheimer (PF) $\left(C_{fs},\ C_{fd}, \phi, r_h\right)$	LTNE (1 equation) $\Delta T = 200$ K	Darcy–Forchheimer (PF) $(C_{fs},\ C_{fd}, \phi, r_h)$	LTNE (1 equation) $T_s = const$	56	Laminar	No steady state	Ansys CFX
[85]	Air	Darcy–Forchheimer (SF) (β, C, ϕ)	LTE $\Delta T = 500$ K	Darcy–Forchheimer (SF) (β, C, ϕ)	LTE $T_p = const$, heat source for HHX	66	$k - \epsilon$	$\approx$ 150 kPa	Ansys Fluent
[69]	Air	Darcy–Forchheimer (PF) $\left(C_{fs}, C_{fd}, \phi, r_h\right)$	LTNE (1 equation) $\Delta T = 200$ K	Darcy–Forchheimer (PF) $(C_{fs},\ C_{fd}, \phi, r_h)$	LTNE (1 equation) $T_s = const$	$\approx$60	Laminar	10,000 Pa	Proprietary
[72]	-	Darcy–Forchheimer (SF) (β, C, ϕ)	LTE	Darcy–Forchheimer (SF) (β, C, ϕ)	LTE Heat source for HHX	22	ILES	>10,000 Pa	Comsol Mult.
[84]	He	Darcy–Forchheimer (SF) (β, C, ϕ)	LTNE (1 equation) $\Delta T = 300$ K	Darcy–Forchheimer (SF) (β, C, ϕ)	LTNE (1 equation) $T_s = const$	114	$k - \epsilon$	-	Ansys Fluent
[143]	He	Darcy–Forchheimer (SF) (β, C, ϕ)	LTE $\Delta T = 300$ K	Darcy–Forchheimer (SF) (β, C, ϕ)	LTE $T_p = const$	76	$k - \epsilon$	550,000 Pa	Ansys Fluent
[144] [145] [146]	He	Darcy–Forchheimer (SF) (β, C, ϕ)	LNTE (2 equations)	Darcy–Forchheimer (SF) (β, C, ϕ)	LNTE (2 equations) $T_{hot} = const$	55–65	-	$T_c \geq 100$ K	CFD-ACE+

Table 6. *Cont.*

Refs.	Fluid	Stack/Regenerator		HX		Frequency [Hz]	Turbulence	Pressure Amp. (or Tcooling/ΔT)	Software
		Momentum	Energy	Momentum	Energy				
[138]	Air	Darcy–Forchheimer (SF) $(\beta, F_\epsilon, \phi)$	LTE	Not considered	Not considered	-	-	$\Delta T \leq 30$ K	Lattice-Boltzmann code
[139]	He	Microscopic	Microscopic, no solid	Darcy–Forchheimer (SF) (β, C, ϕ)	LTE	-	$k - \epsilon$	60,000 Pa	Ansys Fluent
[137]	He	Microscopic	Microscopic CHT $(\Delta T = 587$ K$)$	Darcy–Forchheimer (SF) (β, C, ϕ)	LTE Heat source for HHX, $T_c = 300$ *const*		LES	250,000 Pa	Ansys Fluent

Before concluding this section, it is important to be more specific about HX modeling. At the microscopic scale, the computational costs are not affordable to simulate a full device by taking into account the HXs. Therefore, Ilori et al. experimentally and numerically investigated, with a 3D CFD model, an asymmetric arrangement of a hot HX, surrounded by two identical cold ones. Both experiments and simulations confirmed that at high amplitudes, minor losses caused by sudden area contractions/expansions can be significantly reduced by adopting a specific edge shape, such as the ogive or conic shape, without compromising heat transfer [147,148]. At the macroscopic level, HXs have been modeled with a porous media approach by using the same correlation adopted for regenerators. However, the intrinsic geometric and fluid flow characteristics within HXs are very different from those of a regenerator. Piccolo's works [149,150] demonstrated that there is a strong relation between the hydraulic radius and useful length for a net heat transfer in an HX. In particular, the higher the ratio of r_h/δ_k, the higher the useful length for heat transfer, until $r_h/\delta_k \leq 2$, while, for a regenerator, the hydraulic ratio must be much smaller than the viscous and thermal penetration depths. The same numerical studies have also shown that the optimal length to take advantage of the maximum useful length for heat transfer is about the peak–peak particle displacement. This brings about two reasons for which the classical theory of Swift does not strictly fit in modeling HXs. Firstly, the quasi-steady-state assumption, invoked to resemble the stationary correlations of a regenerator, is not valid because generally $r_h \approx \delta_k$. Secondly, the entrance effects play a significant role because the length of the component and the air particle displacement are comparable.

4.2.3. General Numerical Aspects

In the case of a device solved at the microscopic scale, the mesh criteria are exactly those described for a single TAC. This is in contrast to models with macroscopic porous media, where such criteria may be assessed only at the walls of the empty resonators. With the thermoacoustic phenomena being transient, the time step of the solution needs to be selected accurately taking into account the stability issue and accuracy of reproducing the sinusoidal pattern at the highest meaningful frequency characterizing the thermoacoustic system. For refrigerators driven by a sinusoidal boundary condition (pressure, velocity or moving wall), the fundamental frequency is an intrinsic input of the simulations. For engines, the frequency can only be roughly estimated a priori from the global size of the device and the speed of sound with a purely acoustic approach. As for a single TAC, both the finite element method (FEM) and finite volume method (FVM) in commercial or open-source software have been used. With regard to the FVM-based method, the pressure-based solver with the PISO/PIMPLE algorithms is the most widespread algorithm. Both first- and second-order spatial and time discretization schemes have been used in the literature. With specific reference to the order of the time discretization scheme, it was demonstrated that a first-order scheme is sometimes inaccurate, especially in identifying the onset temperature of a thermoacoustic engine [85,142]. Both explicit (Runge–Kutta) [67,93] and implicit ([97,138]) time schemes have been adopted.

Specific initial conditions, such as the sinusoidal pressure, may accelerate the periodic steady state, especially for thermoacoustic engines. However, this fact should be balanced with the other two additional questions discussed here. Firstly, it was shown that the engine was not able to start up without a small sinusoidal pressure distribution as an initial condition, in the presence of an isothermal boundary condition for the hot HX [83,138]. This problem was not found when a volumetric heat source was used instead of the prescribed temperature for the hot HX. Additionally, in Scalo's work [69], the initial pressure condition could not be lower than 0.5 kPa to promote thermoacoustic instability. At the same time, it cannot be neglected that a thermoacoustic system is a nonlinear bistable system and its solution can strongly depend on the initial conditions [58]. For standing-wave devices, two other possible ways of triggering the thermoacoustic amplification were reviewed by Chen and co-workers [58]. According to the first one (Zink's method [117]), the transient CFD solution has to be initialized by a steady-state solution, where the wall (near the thermal buffer tube) is replaced (just for this step) by a pressure inlet boundary condition. The other method is to prescribe a sinusoidal pressure wave at the other end of the computational domain (pressure outlet). Note that for temperatures higher than the so-called "damping temperature", pressure triggering is not needed, in theory, to start up the engine [58].

5. Conclusions and Future Outlook

In this article, a review of computational thermo-fluid dynamics-based modeling of thermoacoustic phenomena was presented. Even if linear thermoacoustic theory is currently adopted for design purposes of thermoacoustic devices, due to its affordable computational costs, most phenomena characterizing operating conditions of these devices in high-amplitude regimes are intrinsically neglected. In this paper, these phenomena were classified and described, by providing examples of the numerical models available in the literature for each category of nonlinearity. Overall, it has emerged that two approaches are commonly adopted for modeling a thermoacoustic device, depending on the computational domain considered: a single thermoacoustic core or a full device. Concerning single thermoacoustic cores, apart from one exception, they are extracted from a standing-wave thermoacoustic refrigerator to investigate the temperature difference generated across the stack plate ends, or from a standing-wave thermoacoustic engine to evaluate the pressure level reached by imposing a prescribed temperature difference along the stack. These simulations are suitable for performing sensitivity analysis by varying parameters such as the drive ratio, stack length and position, with reasonable computational cost. However, the results, especially for thermoacoustic engines, do not always quantitatively match the results obtained for a full stack. With regard to full devices, the authors proposed a classification between models at the microscopic scale, in which the stack is solved in detail in the numerical simulations, and at the macroscopic scale, where the stack and/or heat exchangers are modeled using a porous media approach. The literature analysis showed that all full devices simulated at the microscopic scale are standing-wave devices, while the thermoacoustic cores of traveling-wave engines are modeled with the porous media correlation used for steady-state flows. This is due to three main reasons:

1. While a traveling-wave thermoacoustic engine works at a low operating frequency and steady-state correlation for porous media can be applied, a standing-wave thermoacoustic engine, working at higher frequencies, requires specific nonlinear correlations in oscillating flows to describe the phase shift between the pressure gradient and velocity, studies on which are currently lacking in the literature.
2. Heat transfer in oscillating flows between the two media in the stack of a standing-wave thermoacoustic engine is irreversible, and a local thermal non-equilibrium model is required.
3. The geometries of regenerators, compared to those of stacks, are irregular and their characteristic lengths are significantly smaller and therefore difficult to be fully modeled without impacting the computational costs.

In conclusion, computational thermo-fluid dynamics is a powerful tool to capture effects that are not considered by linear thermoacoustic theory, to gain a better understanding of the thermoacoustic phenomena and to design devices that operate efficiently under actual conditions. The use of computational thermo-fluid dynamics simulations at the microscopic scale can allow not only reaching higher-fidelity results but also obtaining numerical results that can be exploited (for example, in terms of porous media correlations or minor losses) to improve linear thermoacoustic theory at high amplitudes. The use of macroscopic models for thermoacoustic cores instead represents a good compromise to reduce the computational cost compared to microscopic simulations but is currently not generally applicable to all thermoacoustic devices because the sub-models for porous media are derived from the classical steady-state applications. Further microscopic computational thermo-fluid dynamics simulations or experiments should be aimed at building specific nonlinear porous media correlations that are also valid when steady-state correlations fail.

In addition, whether one considers turbulence models or not in such simulations cannot be underrated. Further numerical and experimental studies are needed to better understand the best turbulent model due to the differences which emerge when adopting different turbulent approaches.

Author Contributions: Conceptualization, A.D.M. and N.M.; methodology, A.D.M. and N.M.; formal analysis, A.D.M.; investigation, A.D.M.; writing—original draft preparation, A.D.M.; writing—review and editing, A.D.M. and N.M.; visualization, A.D.M. and N.M.; supervision, N.M.; project administration, N.M.; funding acquisition, N.M. All authors have read and agreed to the published version of the manuscript.

Funding: This research was funded by Italian Ministry of University and Research (MUR): Project number PRIN 2017JP8PHK.

Conflicts of Interest: The authors declare no conflict of interest.

References

1. JWSB Rayleigh. *The Theory of Sound*; Macmillan and Co., Ltd.: New York, NY, USA, 1896.
2. Abubakar, Z.; Mokheimer, E.M.A.; Kamal, M.M. A Review on Combustion Instabilities in Energy Generating Devices Utilizing Oxyfuel Combustion. *Int. J. Energy Res.* **2021**, *45*, 17461–17479. [CrossRef]
3. Juniper, M.P.; Sujith, R.I. Sensitivity and Nonlinearity of Thermoacoustic Oscillations. *Annu. Rev. Fluid Mech.* **2018**, *50*, 661–689. [CrossRef]
4. Timmer, M.A.G.; De Blok, K.; Van Der Meer, T.H. Review on the Conversion of Thermoacoustic Power into Electricity. *Cit. J. Acoust. Soc. Am.* **2018**, *143*, 841. [CrossRef] [PubMed]
5. Wang, K.; Sanders, S.R.; Dubey, S.; Choo, F.H.; Duan, F. Stirling Cycle Engines for Recovering Low and Moderate Temperature Heat: A Review. *Renew. Sustain. Energy Rev.* **2016**, *62*, 89–108. [CrossRef]
6. Jin, T.; Huang, J.; Feng, Y.; Yang, R.; Tang, K.; Radebaugh, R. Thermoacoustic Prime Movers and Refrigerators: Thermally Powered Engines without Moving Components. *Energy* **2015**, *93*, 828–853. [CrossRef]
7. Steiner, T.W.; Hoy, M.; Antonelli, K.B.; Malekian, M.; Archibald, G.D.S.; Kanemaru, T.; Aitchison, W.; de Chardon, B.; Gottfried, K.T.; Elferink, M.; et al. High-Efficiency Natural Gas Fired 1 KWe Thermoacoustic Engine. *Appl. Therm. Eng.* **2021**, *199*, 117548. [CrossRef]
8. Swift, G.W. *Thermoacoustics: A Unifying Perspective for Some Engines and Refrigerators*, 2nd ed.; Springer: Berlin/Heidelberg, Germany, 2017; ISBN 9783319669328.
9. Avent, A.W.; Bowen, C.R. Principles of Thermoacoustic Energy Harvesting. *Eur. Phys. J. Spec. Top.* **2015**, *224*, 2967–2992. [CrossRef]
10. Pillai, M.A.; Deenadayalan, E. A Review of Acoustic Energy Harvesting. *Int. J. Precis. Eng. Manuf.* **2014**, *15*, 949–965. [CrossRef]
11. Chen, G.; Tang, L.; Mace, B.; Yu, Z. Multi-Physics Coupling in Thermoacoustic Devices: A Review. *Renew. Sustain. Energy Rev.* **2021**, *146*, 111170. [CrossRef]
12. Iniesta, C.; Olazagoitia, J.L.; Vinolas, J.; Aranceta, J. Review of Travelling-Wave Thermoacoustic Electric-Generator Technology. *Proc. Inst. Mech. Eng. Part A J. Power Energy* **2018**, *232*, 940–957. [CrossRef]
13. Zolpakar, N.A.; Mohd-Ghazali, N.; Hassan El-Fawal, M. Performance Analysis of the Standing Wave Thermoacoustic Refrigerator: A Review. *Renew. Sustain. Energy Rev.* **2016**, *54*, 626–634. [CrossRef]
14. Clark, J.P.; Ward, W.C.; Swift, G.W. Design Environment for Low-Amplitude Thermoacoustic Energy Conversion (DeltaEC). *J. Acoust. Soc. Am.* **2007**, *122*, 3014. [CrossRef]
15. Rott, N. Thermoacoustics. *Adv. Appl. Mech.* **1980**, *20*, 135–175.
16. Swift, G.W. Thermoacoustic Engines. *J. Acoust. Soc. Am.* **1988**, *84*, 1145–1180. [CrossRef]
17. Chen, G.; Tang, L.; Mace, B.R. Theoretical and Experimental Investigation of the Dynamic Behaviour of a Standing-Wave Thermoacoustic Engine with Various Boundary Conditions. *Int. J. Heat Mass Transf.* **2018**, *123*, 367–381. [CrossRef]
18. Chen, G.; Tang, L.; Mace, B.R. Modelling and Analysis of a Thermoacoustic-Piezoelectric Energy Harvester. *Appl. Therm. Eng.* **2019**, *150*, 532–544. [CrossRef]
19. Di Meglio, A.; Di Giulio, E.; Dragonetti, R.; Massarotti, N. Analysis of Heat Capacity Ratio on Porous Media in Oscillating Flow. *Int. J. Heat Mass Transf.* **2021**, *179*, 121724. [CrossRef]
20. Swift, G.W. Analysis and Performance of a Large Thermoacoustic Engine. *J. Acoust. Soc. Am.* **1992**, *92*, 1551–1563. [CrossRef]
21. Guedra, M.; Penelet, G. On the Use of a Complex Frequency for the Description of Thermoacoustic Engines. *Acta Acust. united with Acust.* **2012**, *98*, 232–241. [CrossRef]
22. Dan, Z.; Guan, Y. Characterizing Modal Exponential Growth Behaviors of Self-Excited Transverse and Longitudinal Thermoacoustic Instabilities. *Phys. Fluids* **2022**, *34*, 024109. [CrossRef]
23. De Jong, J.A.; Wijnant, Y.H.; De Boer, A. Finite Element Simulation of a Two-Dimensional Standing Wave Thermoacoustic Engine. *Proc. Meet. Acoust.* **2013**, *19*, 030002. [CrossRef]

24. Muralidhar, K.; Suzuki, K. Analysis of Flow and Heat Transfer in a Regenerator Mesh Using a Non-Darcy Thermally Non-Equilibrium Model. *Int. J. Heat Mass Transf.* **2001**, *44*, 2493–2504. [CrossRef]
25. Vafai, K. *Handbook of Porous Media*, 2nd ed.; CRC Press: Boca Raton, FL, USA, 2005; ISBN 9780415876384.
26. Gheisari, R.; Jafarian, A.; Ansari, M.R. Analytical Investigation of Compressible Oscillating Flow in a Porous Media: A Second-Order Successive Approximation Technique. *Int. J. Refrig.* **2012**, *35*, 1789–1799. [CrossRef]
27. Tanaka, M.; Yamashita, I.; Chisaka, F. Flow and Heat Transfer Characteristics of the Stirling Engine Regenerator in an Oscillating Flow. *JSME Int. J.* **1990**, *33*, 283–289. [CrossRef]
28. De Jong, J.A.; Wijnant, J.H.; Wilcox, D.; de Boer, A. Modeling of Thermoacoustic Systems Using the Nonlinear Frequency Domain Method. *J. Acoust. Soc. Am.* **2015**, *138*, 1241. [CrossRef]
29. Yuan, H.; Karpov, S.; Prosperetti, A. A Simplified Model for Linear and Nonlinear Processes in Thermoacoustic Prime Movers. Part II. Nonlinear Oscillations. *J. Acoust. Soc. Am.* **1997**, *102*, 3497–3506. [CrossRef]
30. Watanabe, M.; Prosperetti, A.; Yuan, H. A Simplified Model for Linear and Nonlinear Processes in Thermoacoustic Prime Movers. Part I. Model and Linear Theory. *J. Acoust. Soc. Am.* **1997**, *102*, 3484–3496. [CrossRef]
31. Karpov, S.; Prosperetti, A. A Nonlinear Model of Thermoacoustic Devices. *J. Acoust. Soc. Am.* **2002**, *112*, 1431–1444. [CrossRef]
32. Karpov, S.; Prosperetti, A. Linear Thermoacoustic Instability in the Time Domain. *J. Acoust. Soc. Am.* **2014**, *103*, 3309–3317. [CrossRef]
33. Karpov, S.; Prosperetti, A. Nonlinear Saturation of the Thermoacoustic Instability. *J. Acoust. Soc. Am.* **2000**, *24*, 3130–3147. [CrossRef]
34. Wang, K.; Sun, D.M.; Zhang, J.; Zou, J.; Wu, K.; Qiu, L.M.; Huang, Z.Y. Numerical Simulation on Onset Characteristics of Traveling-Wave Thermoacoustic Engines Based on a Time-Domain Network Model. *Int. J. Therm. Sci.* **2015**, *94*, 61–71. [CrossRef]
35. Swift, G.W.; Ward, W.C. Simple Harmonic Analysis of Regenerators. *J. Thermophys. Heat Transf.* **1996**, *10*, 652–662. [CrossRef]
36. Penelet, G.; Guedra, M.; Gusev, V.; Devaux, T. Simplified Account of Rayleigh Streaming for the Description of Nonlinear Processes Leading to Steady State Sound in Thermoacoustic Engines. *Int. J. Heat Mass Transf.* **2012**, *55*, 6042–6053. [CrossRef]
37. Zare, S.; Tavakolpour-Saleh, A.R. Modeling, Construction, and Testing of a Diaphragm Thermoacoustic Stirling Engine. *Energy Convers. Manag.* **2021**, *243*, 114394. [CrossRef]
38. Matveev, K.I. Unsteady Model for Standing-Wave Thermoacoustic Engines. *J. Non-Equilibrium Thermodyn.* **2010**, *35*, 85–96. [CrossRef]
39. Penelet, G.; Gusev, V.; Lotton, P.; Bruneau, M. Experimental and Theoretical Study of Processes Leading to Steady-State Sound in Annular Thermoacoustic Engines. *Phys. Rev. E - Stat. Nonlinear, Soft Matter Phys.* **2005**, *72*, 1–13. [CrossRef]
40. Guedra, M.; Penelet, G.; Lotton, P. Experimental and Theoretical Study of the Dynamics of Self-Sustained Oscillations in a Standing Wave Thermoacoustic Engine. *J. Appl. Phys.* **2014**, *115*, 024504. [CrossRef]
41. Boroujerdi, A.A.; Ziabasharhagh, M. Investigation of a High Frequency Pulse Tube Cryocooler Driven by a Standing Wave Thermoacoustic Engine. *Energy Convers. Manag.* **2014**, *86*, 194–203. [CrossRef]
42. Sun, D.; Luo, K.; Zhang, J.; Yu, Y.S.W.; Pan, H. A Novel Non-Linear One-Dimensional Unsteady Model for Thermoacoustic Engine and Its Application on a Looped Traveling-Wave Thermoacoustic Engine. *Appl. Acoust.* **2021**, *181*, 108136. [CrossRef]
43. Luo, K.; Zhang, L.; Hu, J.; Luo, E.; Wu, Z.; Sun, Y.; Zhou, Y. Numerical Investigation on a Heat-Driven Free-Piston Thermoacoustic-Stirling Refrigeration System with a Unique Configuration for Recovering Low-to-Medium Grade Waste Heat. *Int. J. Refrig.* **2021**, *130*, 140–149. [CrossRef]
44. Gedeon, D. *Sage User's Guide*; Sage Accpac International, Inc.: Pleasanton, CA, USA, 2021.
45. Li, X.; Liu, B.; Yu, G.; Dai, W.; Hu, J.; Luo, E.; Li, H. Experimental Validation and Numeric Optimization of a Resonance Tube-Coupled Duplex Stirling Cooler. *Appl. Energy* **2017**, *207*, 604–612. [CrossRef]
46. Gary, J.; O'Gallagher, A.; Radebaugh, R. *A Numerical Model for Regenerator Performance*; Technical Report; NIST: Boulder, CO, USA, 1994.
47. Li, Z.F.; Qiu, L.M.; Liu, G.J.; Wang, B.; Hu, J.-Q. Simulation and Experimental Study of Pulse Tube Cooler Driven by Thermoacoustic Engine. *J. Zhejiang Univ.* **2009**, *43*, 1458–1462.
48. Marx, D.; Blanc-Benon, P. Computation of the Temperature Distortion in the Stack of a Standing-Wave Thermoacoustic Refrigerator. *J. Acoust. Soc. Am.* **2005**, *118*, 2993–2999. [CrossRef]
49. Gusev, V.; Hélène, B.; Pierrick, L.; Stéphane, J.; Bruneau, M. Enhancement of the Q of a Nonlinear Acoustic Resonator by Active Suppression of Harmonics. *J. Acoust. Soc. Am.* **1998**, *12*, 177–179. [CrossRef]
50. Gupta, P.; Lodato, G.; Scalo, C. Numerical Investigation and Modeling of Thermoacoustic Shock Waves. In Proceedings of the AIAA SciTech Forum-55th AIAA Aerospace Scinces Meeting, Grapevine, TX, USA, 9–13 January 2017. [CrossRef]
51. Gupta, P.; Lodato, G.; Scalo, C. Spectral Energy Cascade in Thermoacoustic Shock Waves. *J. Fluid Mech.* **2017**, *831*, 358–393. [CrossRef]
52. Olivier, C.; Penelet, G.; Poignand, G.; Gilbert, J.; Lotton, P. Weakly Nonlinear Propagation in Thermoacoustic Engines: A Numerical Study of Higher Harmonics Generation up to the Appearance of Shock Waves. *Acta Acust. United Acust.* **2015**, *101*, 941–949. [CrossRef]
53. Biwa, T.; Takahashi, T.; Yazaki, T. Observation of Traveling Thermoacoustic Shock Waves (L). *J. Acoust. Soc. Am.* **2011**, *130*, 3558–3561. [CrossRef]

54. Hantschk, C.C.; Vortmeyer, D. Numerical Simulation of Self-Excited Thermoacoustic Instabilities in a Rijke Tube. *J. Sound Vib.* **1999**, *227*, 511–522. [CrossRef]
55. Chen, G.; Tang, L.; Yu, Z. Underlying Physics of Limit-Cycle, Beating and Quasi-Periodic Oscillations in Thermoacoustic Devices. *J. Phys. D Appl. Phys.* **2020**, *53*, 215502. [CrossRef]
56. Delage, R.; Takayama, Y.; Hyodo, H.; Biwa, T. Observation of Thermoacoustic Chaotic Oscillations in a Looped Tube. *Chaos* **2019**, *29*, 093108. [CrossRef]
57. Chen, G.; Tang, L.; Yu, Z.; Mace, B. Mode Transition in a Standing-Wave Thermoacoustic Engine: A Numerical Study. *J. Sound Vib.* **2021**, *504*, 116119. [CrossRef]
58. Chen, G.; Tang, L.; Mace, B.R. Bistability and Triggering in a Thermoacoustic Engine: A Numerical Study. *Int. J. Heat Mass Transf.* **2020**, *157*, 119951. [CrossRef]
59. Chen, M.; Ju, Y.L. Experimental Study of Quasi-Periodic on-off Phenomena in a Small-Scale Traveling Wave Thermoacoustic Heat Engine. *Cryogenics* **2017**, *85*, 23–29. [CrossRef]
60. Yu, Z.; Jaworski, A.J.; Abduljalil, A.S. Fishbone-like Instability in a Looped-Tube Thermoacoustic Engine. *J. Acoust. Soc. Am.* **2010**, *128*, EL188–EL194. [CrossRef] [PubMed]
61. Feldmann, D.; Wagner, C. Direct Numerical Simulation of Fully Developed Turbulent and Oscillatory Pipe Flows at Reτ = 1440. *J. Turbul.* **2012**, *13*, 1–28. [CrossRef]
62. Hino, M.; Sawamoto, M.; Takasu, S. Experiments on Transition to Turbulence in an Oscillatory Pipe Flow. *J. Fluid Mech.* **1976**, *75*, 193–207. [CrossRef]
63. Seume, J.; Friedman, G.; Simon, T.W. *Fluid Mechanics Experiments in Oscillatory Flow*; Technical report NASA CR-189127; NASA: Washington, DC, USA, 1992.
64. Simon, T.W.; Ibrahim, M.; Kannapareddy, M.; Johnson, T.; Friedman, G. Transition of Oscillatory Flow in Tubes: An Empirical Model for Application to Stirling Engines. *SAE Tech. Pap.* **1992**. [CrossRef]
65. Mohd Saat, F.A.Z.; Jaworski, A.J. Numerical Predictions of Early Stage Turbulence in Oscillatory Flow across Parallel-Plate Heat Exchangers of a Thermoacoustic System. *Appl. Sci.* **2017**, *7*, 673. [CrossRef]
66. Huang, H.; Jaworski, A. Numerical Simulation of the Effect of Plate Spacing on Heat Transfer Characteristics within a Parallel-Plate Heat Exchanger in a Standing Wave Thermoacoustic System. *E3S Web Conf.* **2019**, *116*, 00028. [CrossRef]
67. Ramadan, I.; Essawey, A.H.I.; Abdel-rahman, E. Transition to Turbulence in Oscillating Flow. In Proceedings of the 24th International Congress on Sound and Vibration, London, UK, 23–27 July 2017.
68. Merkli, P.; Thomann, H. Transition to Turbulence in Oscillating Pipe Flow. *J. Fluid Mech.* **1975**, *68*, 567–576. [CrossRef]
69. Scalo, C.; Lele, S.K.; Hesselink, L. Linear and Nonlinear Modelling of a Theoretical Travelling-Wave Thermoacoustic Heat Engine. *J. Fluid Mech.* **2015**, *766*, 368–404. [CrossRef]
70. Lin, J.; Scalo, C.; Hesselink, L. High-Fidelity Simulation of a Standing-Wave Thermoacoustic-Piezoelectric Engine. *J. Fluid Mech.* **2016**, *808*, 19–60. [CrossRef]
71. Mahdaoui, M.; Bennacer, R.; Kouidri, S.; Martaj, N. Numerical Investigation of Thermoacoustic Engine Using Implicit Large Eddy Simulation. In Proceedings of the 7th European Congress on Computational Methods in Applied Sciences and Engineering, Crete Island, Greece, 5–10 June 2016; Volume 4, pp. 7609–7619. [CrossRef]
72. Ali, M.M.; Martaj, N.; Laaouatni, A.; Savarese, S.; Bennacer, R.; Kouidri, S. 2D Simulation of the Oscillating Flow in the Thermoacoustic Engine Swift Backhaus. In Proceedings of the International Renewable and Sustainable Energy Conference (IRSEC), Marrakech, Morocco, 14–17 November 2016; pp. 862–865. [CrossRef]
73. Ahn, K.H.; Ibrahim, M.B. Laminar/Turbulent Oscillating Flow in Circular Pipes. *Int. J. Heat Fluid Flow* **1992**, *13*, 340–346. [CrossRef]
74. Chen, G.; Wang, Y.; Tang, L.; Wang, K.; Yu, Z. Large Eddy Simulation of Thermally Induced Oscillatory Flow in a Thermoacoustic Engine. *Appl. Energy* **2020**, *276*, 115458. [CrossRef]
75. Jaworski, A.J.; Mao, X.; Mao, X.; Yu, Z. Entrance Effects in the Channels of the Parallel Plate Stack in Oscillatory Flow Conditions. *Exp. Therm. Fluid Sci.* **2009**, *33*, 495–502. [CrossRef]
76. Lixian, G.; Dan, Z.; Sid, B. Temperature Difference and Stack Plate Spacing Effects on Thermodynamic Performances of Standing-Wave Thermoacoustic Engines Driven by Cryogenic Liquids and Waste Heat. *J. Therm. Sci.* **2022**, *31*, 1–18.
77. Spalart, P.R. Detached-Eddy Simulation. *Annu. Rev. Fluid Mech.* **2009**, *41*, 181–202. [CrossRef]
78. Boluriaan, S.; Morris, P.J. Acoustic Streaming: From Rayleigh to Today. *Int. J. Aeroacoustics* **2003**, *2*, 255–292. [CrossRef]
79. Oosterhuis, J.P.; Bühler, S.; Wilcox, D.; Van Der Meer, T.H. Computational Fluid Dynamics Simulation of Rayleigh Streaming in a Vibrating Resonator. *Proc. Meet. Acoust.* **2013**, *19*, 030008. [CrossRef]
80. Chen, G.; Krishan, G.; Yang, Y.; Tang, L.; Mace, B. Numerical Investigation of Synthetic Jets Driven by Thermoacoustic Standing Waves. *Int. J. Heat Mass Transf.* **2020**, *146*, 118859. [CrossRef]
81. Shi, L.; Yu, Z.; Jaworski, A.J. Vortex Shedding Flow Patterns and Their Transitions in Oscillatory Flows Past Parallel-Plate Thermoacoustic Stacks. *Exp. Therm. Fluid Sci.* **2010**, *34*, 954–965. [CrossRef]
82. Olson, J.R.; Swift, G.W. Energy Dissipation in Oscillating Flow through Straight and Coiled Pipes. *J. Acoust. Soc. Am.* **1996**, *100*, 2123–2131. [CrossRef]
83. Yiyi, M.; Xiujuan, X.; Shaoqi, Y.; Qing, L. Study on Minor Losses around the Thermoacoustic Parallel Stack in the Oscillatory Flow Conditions. *Phys. Procedia* **2015**, *67*, 485–490. [CrossRef]

84. Lycklama À Nijeholt, J.A.; Tijani, M.E.H.; Spoelstra, S.; Loginov, M.S.; Kuczaj, A.K. CFD Modeling of Streaming Phenomena in a Torus-Shaped Thermoacoustic Engine. In Proceedings of the 19th International Congress on Sound and Vibration, ICSV 2012, Vilnius, Lithuania, 8–12 July 2012; Volume 3, pp. 2024–2031.
85. Yu, G.Y.; Luo, E.C.; Dai, W.; Hu, J.Y. Study of Nonlinear Processes of a Large Experimental Thermoacoustic- Stirling Heat Engine by Using Computational Fluid Dynamics. *J. Appl. Phys.* **2007**, *102*, 074901. [CrossRef]
86. Yang, P.; Chen, H.; Liu, Y. Numerical Investigation on Nonlinear Effect and Vortex Formation of Oscillatory Flow throughout a Short Tube in a Thermoacoustic Stirling Engine. *J. Appl. Phys.* **2017**, *121*, 214902. [CrossRef]
87. Backhaus, S.; Swift, G.W. A Thermoacoustic-Stirling Heat Engine: Detailed Study. *J. Acoust. Soc. Am.* **2000**, *107*, 3148–3166. [CrossRef]
88. Boluriaan, S.; Morris, P.J. Suppression of Traveling Wave Streaming Using a Jet Pump. In Proceedings of the 41st Aerospace Sciences Meeting and Exhibit, Reno, NV, USA, 6–9 January 2003.
89. Oosterhuis, J.P.; Bühler, S.; van der Meer, T.H.; Wilcox, D. A Numerical Investigation on the Vortex Formation and Flow Separation of the Oscillatory Flow in Jet Pumps. *J. Acoust. Soc. Am.* **2015**, *137*, 1722–1731. [CrossRef]
90. Timmer, M.A.G.; Oosterhuis, J.P.; Bühler, S.; Wilcox, D.; van der Meer, T.H. Characterization and Reduction of Flow Separation in Jet Pumps for Laminar Oscillatory Flows. *J. Acoust. Soc. Am.* **2016**, *139*, 193–203. [CrossRef]
91. Oosterhuis, J.P.; Verbeek, A.A.; Bühler, S.; Wilcox, D.; van der Meer, T.H. Flow Separation and Turbulence in Jet Pumps for Thermoacoustic Applications. *Flow, Turbul. Combust.* **2017**, *98*, 311–326. [CrossRef]
92. Ohmi, M.; Iguchi, M. Critical Reynolds Number in an Oscillating Pipe Flow. *Bull. JSME* **1982**, *25*, 165–172. [CrossRef]
93. Rahpeima, R.; Ebrahimi, R. Numerical Investigation of the Effect of Stack Geometrical Parameters and Thermo-Physical Properties on Performance of a Standing Wave Thermoacoustic Refrigerator. *Appl. Therm. Eng.* **2019**, *149*, 1203–1214. [CrossRef]
94. Mergen, S.; Yıldırım, E.; Turkoglu, H. Numerical Study on Effects of Computational Domain Length on Flow Field in Standing Wave Thermoacoustic Couple. *Cryogenics* **2019**, *98*, 139–147. [CrossRef]
95. Marx, D.; Blanc-Benon, P. Numerical Calculation of the Temperature Difference between the Extremities of a Thermoacoustic Stack Plate. *Cryogenics* **2005**, *45*, 163–172. [CrossRef]
96. Worlikar, A.S.; Knio, O.M.; Klein, R. Numerical Simulation of a Thermoacoustic Refrigerator. *J. Comput. Phys.* **1998**, *144*, 299–324. [CrossRef]
97. Marx, D.; Blanc-Benon, P. Numerical Simulation of Stack-Heat Exchangers Coupling in a Thermoacoustic Refrigerator. *AIAA J.* **2004**, *42*, 1338–1347. [CrossRef]
98. Zoontjens, L.; Howard, C.Q.; Zander, A.C.; Cazzolato, B.S. Numerical Study of Flow and Energy Fields in Thermoacoustic Couples of Non-Zero Thickness. *Int. J. Therm. Sci.* **2009**, *48*, 733–746. [CrossRef]
99. El-Rahman, A.I.A.; Abdel-Rahman, E. Computational Fluid Dynamics Simulation of a Thermoacoustic Refrigerator. *J. Thermophys. Heat Transf.* **2014**, *28*, 78–86. [CrossRef]
100. Namdar, A.; Kianifar, A.; Roohi, E. Numerical Investigation of Thermoacoustic Refrigerator at Weak and Large Amplitudes Considering Cooling Effect. *Cryogenics* **2015**, *67*, 36–44. [CrossRef]
101. Cao, N.; Olson, J.R.; Swift, G.W.; Chen, S. Energy Flux Density in a Thermoacoustic Couple. *J. Acoust. Soc. Am.* **1996**, *99*, 3456–3464. [CrossRef]
102. Ishikawa, H.; Mee, D.J. Numerical Investigations of Flow and Energy Fields near a Thermoacoustic Couple. *J. Acoust. Soc. Am.* **2002**, *111*, 831–839. [CrossRef]
103. Ke, H.B.; Liu, Y.W.; He, Y.L.; Wang, Y.; Huang, J. Numerical Simulation and Parameter Optimization of Thermo-Acoustic Refrigerator Driven at Large Amplitude. *Cryogenics* **2010**, *50*, 28–35. [CrossRef]
104. Tasnim, S.H.; Fraser, R.A. Computation of the Flow and Thermal Fields in a Thermoacoustic Refrigerator. *Int. Commun. Heat Mass Transf.* **2010**, *37*, 748–755. [CrossRef]
105. Abd El-Rahman, A.I.; Abdelfattah, W.A.; Fouad, M.A. A 3D Investigation of Thermoacoustic Fields in a Square Stack. *Int. J. Heat Mass Transf.* **2017**, *108*, 292–300. [CrossRef]
106. Worlikar, A.S.; Knio, O.M.; Klein, R. Numerical study of oscillatory flow and heat transfer in a loaded thermoacoustic stack. *Int. J. Comput. Methodol.* **1999**, *35*, 49–65. [CrossRef]
107. Boroujerdi, A.A.; Ziabasharhagh, M. A Coupled Computational Model of Nonlinear Thermoacoustics of Standing Wave Heat Engines. *Heat Mass Transf. Stoffuebertragung* **2019**, *55*, 3223–3241. [CrossRef]
108. Migliorino, M.T.; Scalo, C. Real Fluid Effects Thermoacoustic Engine.Pdf. *J. Fluid Mech.* **2019**, *883*, A23. [CrossRef]
109. Marx, D.; Blanc-Benon, P. Numerical Simulation of the Coupling between Stack and Heat Exchangers in a Thermoacoustic Refrigerator. In Proceedings of the 9th AIAA/CEAS Aeroacoustics Conference and Exhibit, Hilton Head, CA, USA, 12–14 May 2003. [CrossRef]
110. Hamilton, M.F.; Ilinskii, Y.A.; Zabolotskaya, E.A. Nonlinear Two-Dimensional Model for Thermoacoustic Engines. *J. Acoust. Soc. Am.* **2002**, *111*, 2076. [CrossRef]
111. Ja'fari, M.; Jaworski, A.J.; Piccolo, A.; Simpson, K. Numerical Study of Transient Characteristics of a Standing-Wave Thermoacoustic Heat Engine. *Int. J. Heat Mass Transf.* **2022**, *186*, 122530. [CrossRef]
112. Sharify, E.M.; Takahashi, S.; Hasegawa, S. Development of a CFD Model for Simulation of a Traveling-Wave Thermoacoustic Engine Using an Impedance Matching Boundary Condition. *Appl. Therm. Eng.* **2016**, *107*, 1026–1035. [CrossRef]
113. Rogoziński, K.; Nowak, I.; Nowak, G. Modeling the Operation of a Thermoacoustic Engine. *Energy* **2017**, *138*, 249–256. [CrossRef]

114. Nowak, I.; Rulik, S.; Wróblewski, W.; Nowak, G.; Szwedowicz, J. Analytical and Numerical Approach in the Simple Modelling of Thermoacoustic Engines. *Int. J. Heat Mass Transf.* **2014**, *77*, 369–376. [CrossRef]
115. Zink, F.; Vipperman, J.S.; Schaefer, L.A. Advancing Thermoacoustics through CFD Simulation Using Fluent. *ASME Int. Mech. Eng. Congr. Expo. Proc.* **2009**, *8*, 101–110. [CrossRef]
116. Zink, F.; Vipperman, J.; Schaefer, L. CFD Simulation of a Thermoacoustic Engine with Coiled Resonator. *Int. Commun. Heat Mass Transf.* **2010**, *37*, 226–229. [CrossRef]
117. Zink, F.; Vipperman, J.; Schaefer, L. CFD Simulation of Thermoacoustic Cooling. *Int. J. Heat Mass Transf.* **2010**, *53*, 3940–3946. [CrossRef]
118. Skaria, M.; Abdul Rasheed, K.K.; Shafi, K.A.; Kasthurirengan, S.; Behera, U. Simulation Studies on the Performance of Thermoacoustic Prime Movers and Refrigerator. *Comput. Fluids* **2015**, *111*, 127–136. [CrossRef]
119. Ali, U.; Abedrabbo, S.; Janajreh, I. Numerical Simulation of Thermoacoustic Refrigerator Coupled with Thermoacoustic Engine. In Proceedings of the 15th International Conference On Heat Transfer, Fluid Mechanics and Thermodynamics (HEFAT), Virtual, 25–27 July 2021.
120. Bouramdane, Z.; Bah, A.; Alaoui, M.; Martaj, N. Numerical Analysis of Thermoacoustically Driven Thermoacoustic Refrigerator with a Stack of Parallel Plates Having Corrugated Surfaces. *Int. J. Air-Cond. Refrig.* **2022**, *30*, 1–19. [CrossRef]
121. Chen, G.; Li, Z.; Tang, L.; Yu, Z. Mutual Synchronization of Self-Excited Acoustic Oscillations in Coupled Thermoacoustic Oscillators. *J. Phys. D. Appl. Phys.* **2021**, *54*, 48. [CrossRef]
122. Rogoziński, K.; Nowak, G. Numerical Investigation of Dual Thermoacoustic Engine. *Energy Convers. Manag.* **2020**, *203*, 112231. [CrossRef]
123. Bouramdane, Z.; Hafs, H.; Bah, A.; Alaoui, M.; Martaj, N.; Savarese, S. Standing Wave Thermoacoustic Refrigerator: The Principle of Thermally Driven Cooling. In Proceedings of the 6th International Renewable and Sustainable Energy Conference (IRSEC), Rabat, Morocco, 5–8 December 2018; pp. 1–6. [CrossRef]
124. Muralidharan, H.; Hariharan, N.M.; Perarasu, V.T.; Sivashanmugam, P.; Kasthurirengan, S. CFD Simulation of Thermoacoustic Heat Engine. *Prog. Comput. Fluid Dyn.* **2014**, *14*, 131–137. [CrossRef]
125. Kuzuu, K.; Hasegawa, S. Numerical Investigation of Heated Gas Flow in a Thermoacoustic Device. *Appl. Therm. Eng.* **2017**, *110*, 1283–1293. [CrossRef]
126. Kuzuu, K.; Hasegawa, S. Effect of Non-Linear Flow Behavior on Heat Transfer in a Thermoacoustic Engine Core. *Int. J. Heat Mass Transf.* **2017**, *108*, 1591–1601. [CrossRef]
127. Chen, G.; Wang, Y.; Tang, L.; Wang, K.; Mace, B.R. Large Eddy simulation of self-excited acoustic oscillations in a thermoacoustic engine. In Proceedings of the International Conference on Applied Energy, Västerås, Sweden, 12–15 August 2019; pp. 1–5.
128. Gupta, S.K.; Ghosh, P.; Nandi, T.K. Theoretical and CFD Investigations on a 200 Hz Thermoacoustic Heat Engine Using Pin Array Stack for Operations in a Pulse Tube Cryocooler. *IOP Conf. Ser. Mater. Sci. Eng.* **2019**, *502*, 012025. [CrossRef]
129. Zhang, Y.; Shi, X.; Li, Y.; Zhang, Y.; Liu, Y. Characteristics of Thermoacoustic Conversion and Coupling Effect at Different Temperature Gradients. *Energy* **2020**, *197*, 117228. [CrossRef]
130. Harikumar, G.; Shen, L.; Wang, K.; Dubey, S.; Duan, F. Transfer Transient Thermofluid Simulation of a Hybrid Thermoacoustic System. *Int. J. Heat Mass Transf.* **2022**, *183*, 122181. [CrossRef]
131. Luo, J.; Zhou, Q.; Jin, T. Numerical Simulation of Nonlinear Phenomena in a Standing-Wave Thermoacoustic Engine with Gas-Liquid Coupling Oscillation. *Appl. Therm. Eng.* **2022**, *207*, 118131. [CrossRef]
132. Tisovsky, T.; Vit, T. Design of Numerical Model for Thermoacoustic Devices Using OpenFOAM. *AIP Conf. Proc.* **2017**, *1889*, 020043. [CrossRef]
133. Chen, G.; Hao, H.; Deng, A. Linear and Nonlinear Modeling of Self-Excited Acoustic Oscillations in a T-Shaped Thermoacoustic Engine. *AIP Adv.* **2021**, *11*, 085120. [CrossRef]
134. Whitaker, S. Flow in Porous Media I: A Theoretical Derivation of Darcy's Law. *Transp. Porous Media* **1986**, *1*, 3–25. [CrossRef]
135. Whitaker, S. The Forchheimer Equation: A Theoretical Development. *Transp. Porous Media* **1996**, *25*, 27–61. [CrossRef]
136. Pati, S.; Borah, A.; Boruah, M.P.; Randive, P.R. Critical Review on Local Thermal Equilibrium and Local Thermal Non-Equilibrium Approaches for the Analysis of Forced Convective Flow through Porous Media. *Int. Commun. Heat Mass Transf.* **2022**, *132*, 105889. [CrossRef]
137. Miled, O.; Dhahri, H.; Mhimid, A. Numerical Investigation of Porous Stack for a Solar-Powered Thermoacoustic Refrigerator. *Adv. Mech. Eng.* **2020**, *12*, 1–14. [CrossRef]
138. Yu, G.; Dai, W.; Luo, E. CFD Simulation of a 300 Hz Thermoacoustic Standing Wave Engine. *Cryogenics* **2010**, *50*, 615–622. [CrossRef]
139. Liu, L.; Yang, P.; Liu, Y. Comprehensive Performance Improvement of Standing Wave Thermoacoustic Engine with Converging Stack: Thermodynamic Analysis and Optimization. *Appl. Therm. Eng.* **2019**, *160*, 114096. [CrossRef]
140. ESI-CFD-Inc. CFD-ACE+ V2009.4. In *User Manual*; ESI Group: Hunstville, AL, USA, 2009.
141. Tew, R.; Simon, T.; Gedeon, D.; Ibrahim, M.; Rong, W. An Initial Non-Equilibrium Porous-Media Model for CFD Simulation of Stirling Regenerators. In Proceedings of the 4th International Energy Conversion Engineering Conference and Exhibit, San Diego, CA, USA, 26–29 June 2006; Volume 1, pp. 65–77. [CrossRef]
142. Lycklama à Nijeholt, J.A.; Tijani, M.E.H.; Spoelstra, S. Simulation of a Traveling-Wave Thermoacoustic Engine Using Computational Fluid Dynamics. *J. Acoust. Soc. Am.* **2005**, *118*, 2265–2270. [CrossRef]

143. Liu, L.; Liu, Y.; Duan, F. Effect of the Characteristic Time on the System Performance of a Three-Stage Looped Traveling-Wave Thermoacoustic Engine. *Energy Convers. Manag.* **2020**, *224*, 113367. [CrossRef]
144. Antao, D.S.; Farouk, B. Experimental and Numerical Investigations of an Orifice Type Cryogenic Pulse Tube Refrigerator. *Appl. Therm. Eng.* **2013**, *50*, 112–123. [CrossRef]
145. Antao, D.S.; Farouk, B. Computational Fluid Dynamics Simulations of an Orifice Type Pulse Tube Refrigerator: Effects of Operating Frequency. *Cryogenics* **2011**, *51*, 192–201. [CrossRef]
146. Antao, D.S.; Farouk, B. Numerical Simulations of Transport Processes in a Pulse Tube Cryocooler: Effects of Taper Angle. *Int. J. Heat Mass Transf.* **2011**, *54*, 4611–4620. [CrossRef]
147. Ilori, O.M.; Jaworski, A.J.; Mao, X.; Ismail, O.S. Effects of Edge Shapes on Thermal-Fluid Processes in Oscillatory Flows. *Therm. Sci. Eng. Prog.* **2021**, *25*, 101004. [CrossRef]
148. Ilori, O.M.; Jaworski, A.J.; Mao, X. Experimental and Numerical Investigations of Thermal Characteristics of Heat Exchangers in Oscillatory Flow. *Appl. Therm. Eng.* **2018**, *144*, 910–925. [CrossRef]
149. Piccolo, A. Numerical Computation for Parallel Plate Thermoacoustic Heat Exchangers in Standing Wave Oscillatory Flow. *Int. J. Heat Mass Transf.* **2011**, *54*, 4518–4530. [CrossRef]
150. Piccolo, A.; Pistone, G. Estimation of Heat Transfer Coefficients in Oscillating Flows: The Thermoacoustic Case. *Int. J. Heat Mass Transf.* **2006**, *49*, 1631–1642. [CrossRef]